2022-12-19

DISEÑO E IMPLEMENTACIÓN DE CONTROL PREDICTIVO CON MODULACIÓN VECTORIAL EN UN CONVERTIDOR DE POTENCIA DE CUATRO PIERNAS

LEIVA SILVA, FELIPE IGNACIO

Universidad Técnica Federico Santa María

Departamento Ingeniería Eléctrica

DISEÑO E IMPLEMENTACIÓN DE CONTROL PREDICTIVO CON MODULACIÓN VECTORIAL EN UN CONVERTIDOR DE POTENCIA DE CUATRO PIERNAS

MEMORIA DE TITULACIÓN PARA OPTAR AL TÍTULO DE INGENIERO CIVIL ELECTRICISTA

Felipe Ignacio Leiva Silva

Profesor Guía
Dr. Andrés Mora Castro

Co-referentes
Dr. Roberto Cárdenas Dobson
Dr. Matías Urrutia Ortiz

December 19, 2022

Acknowledgement

First of all, I want to thank my parents, and brother, who have always supported me in all the decisions I have made in my life, whether they are good or bad, they are always there to comfort me and give me the necessary advice so that I can always move forward. I am lucky to have such a wonderful family, I love you so much.

To my brother from another mother, Francisco San Martin, who has been an uninterrupted part of my life. We've known each other practically our entire lives, you're my best friend and you've always been with me, not only to laugh and have a good time but also in those moments when I need someone else to listen to me. You helped me grow personally and believe it or not, you have taught me many of the things that make me the person I am today.

To my school friends that I have managed to keep all this time. People always say that it is strange that I still have contact with them at this point in life, and even more, that we are so close. My affection and love for you is unconditional. I hope this relationship continues for a lifetime regardless of whether each of us follows our own path. Because I know that even if we don't see each other for a long time when we meet again it will be as if time had not passed.

To my university classmates, who know better than them how difficult it was to overcome this stage, however, that did not prevent us from finding moments to enjoy all those very complex semesters. I hope, as with everyone else, that our relationship lasts forever.

To my girlfriend Paula Lopez, although you appeared in my life relatively recently compared to the others, I want to thank you for your support and love over all these months. The love that you give me and your dedication make everything worth it. I appreciate having met you and that you are part of my life, I am very happy by your side and I love you so much.

Finally, I want to thank my professors, especially Andrés Mora, for allowing me to work with him and for giving me help and support throughout the work. Also to Professor Roberto Cárdenas for allowing me to work on the premises of the University of Chile. And to Professor Matías Urrutia for all his help when I arrived at the laboratory and faced this challenge for the first time.

Contents

List of Figures

List of Tables

Glossary

3P3W Three-Phase Three-Wire. 9, 19

3P4W Three-Phase Four-Wire. 9, 19, 20

4L-2L Four-Leg Two-Level. 5, 7, 11, 15, 16, 20–23, 29

AC Alternate Current. 18

CCS Continuous Control Set. 12–14

DC Direct Current. 18

DN Distributed Network. 9

FCS Finite Control Set. 10–12, 14, 25, 29

MG Micro Grid. 9

MPC Model Predictive Control. 5, 10–15, 26–29

OSS Optimal Switching Sequence. 14, 15, 26–30, 36

OSV Optimal Switching Vector. 14

PR Proportional Resonant. 33

RE Renewable Energy. 9

UASV Unconstrained Average Switching Vector. 28

VSC Voltage Source Converter. 5, 10, 11, 19–21, 26

Chapter 1

Introduction

The general structure of an electrical interconnected system is presented in Fig. 1.1. It can be divided into three main sectors: generation, transmission and distribution systems. The interconnection of several generation units to provide energy to the end consumers sets up a complex network. In this large systems the active power delivered by generators can be directly associated to the control of the system frequency and the reactive power, along with the use of reactive passive elements, is associated to the control of voltage magnitude at the different nodes of the electrical system.

The utility industry across the world is trying to address numerous challenges, including generation diversification, optimal deployment of expensive assets, demand response, energy conservation, and reduction of the industry overall carbon footprint. It is evident that such critical issues cannot be addressed within the confines of the existing electricity grid. The existing electricity grid is unidirectional in nature. In this hierarchical configuration, a failure in any component is transferred to other components in the chain and may result in poor power quality, such as power cuts or even blackouts. [3]

However, this traditional scheme of the electrical system has been slowly disrupted thanks to the integration of variable renewable energy (RE) resources (like photovoltaic and wind, and energy storage systems) into distributed networks (DN) and microgrids (MG), emerging as a key issue in the ongoing energy transition [4–6]. Low voltage MGs and DNs are typically unbalanced electric grids [7, 8], and their network structures are: (i) three-phase three-wire (3P3W) and (ii) three-phase four-wire (3P4W) systems.

The four-leg converter topology is a promising solution compared with the three-leg inverters with split DC-bus to solve the output power quality issues and achieve transformerless operation [9]. The output current control of this converter topology is a critical aspect in 3P4W applications such as distributed generation (DG) units [10], shunt active filters [11–13], and sharing of unbalanced load in microgrids [14]. Ac-

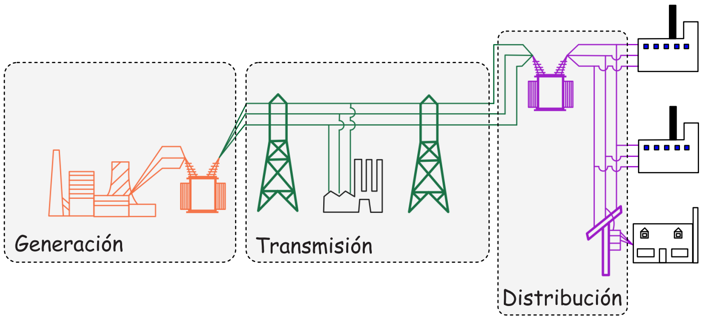

Figure 1.1: Representation of a typical electrical system

cordingly, some of the desired features of the current control are (i) accurate current control; (ii) high bandwidth; (iii) fast dynamic response; and (iv) low harmonic distortion. Aiming to fulfill these features, many control strategies such as proportional-integral (PI) controllers in synchronous reference frames, proportional-resonant (PR) controllers, repetitive controllers (RC), deadbeat and model predictive controllers, among others, have been proposed in the literature [15].

PR controllers [16] are applied for effective tracking of the fundamental current references, while multi-resonant (MR) controllers tuned at specific harmonic frequencies are adopted for tracking selected harmonics in the current references [10,17]. However, the PR-based control structures show some limitations when the reference currents have rich-content harmonics (as in the case of active-filter applications). Firstly, undesired dynamic response due to poles and zeros coupling of the transfer function resulting from multiple PR controllers tuned individually at each harmonic frequency; secondly, anti-windup structures for MR controllers are effective but not optimal from the control point of view; and thirdly, the need to implement leading/lag compensation methods to ensure stability and adequate current tracking performance at high frequencies [17].

The development of more powerful microprocessors has motivated the exploration of more sophisticated strategies to control power converters. In this scenario, model predictive control (MPC) has established itself as a promising control methodology. In power electronics, it is convenient to classify MPC methods depending on how the switching devices are controlled and, consequently, the underlying optimization problem for computing the optimal control actions [1,18,19]. Due to its well-reported advantages such as intuitive design procedure, straightforward implementation, and favorable system performance, one of the most attractive MPC strategies is the so-called finite control set MPC (FCS-MPC) [20].

The FCS-MPC directly uses the switching vectors of the power converter to define the feasible control set. Thus, the optimization algorithm aims to find the optimal switching action which minimizes a given cost function quantifying the tracking error and switching effort. This FCS-MPC approach has been introduced in [9,11,21,22] for currents tracking control in 4-leg grid-connected voltage source converters (VSC) and active filter applications. In this regard, the design and tuning of the internal current control loop along with the implementation of a modulation stage can be avoided with no negative effect on the steady-state operation and transients. However, weighting factors are required to trade-off the switching effort and the tracking error. Moreover, it generates a variable switching frequency, producing dispersed harmonic spectra in the output voltages, and higher ripple in the currents than produced by techniques that include modulation stages at similar switching frequencies [23].

Motivated by the concerns mentioned above, this work presents a flexible and versatile model predictive current controller based on the optimal switching sequences concept for 4-leg 2-level (4L-2L) grid-connected power converters. The proposed MPC controller explicitly considers the modulator in its formulation along with the prediction model of the average trajectory of the variables to be controlled. The key novelty of this proposal lies in that the control algorithm determines the optimal tetrahedron and the application times of its switching vectors to provide the optimal switching sequence. Consequently, the resulting MPC strategy enables the reduction of the harmonic distortion in the variable of concern and achieves the operation of the power converter at a fixed switching frequency, thus resulting in deterministic and reduced switching losses. Moreover, the proposed MPC controller establishes well-defined output voltage spectra without compromising the inherent fast dynamic responses of the FCS-MPC strategy. These advantages make the proposed controller useful for both shunt active filter applications and DG systems with unbalanced power injection.

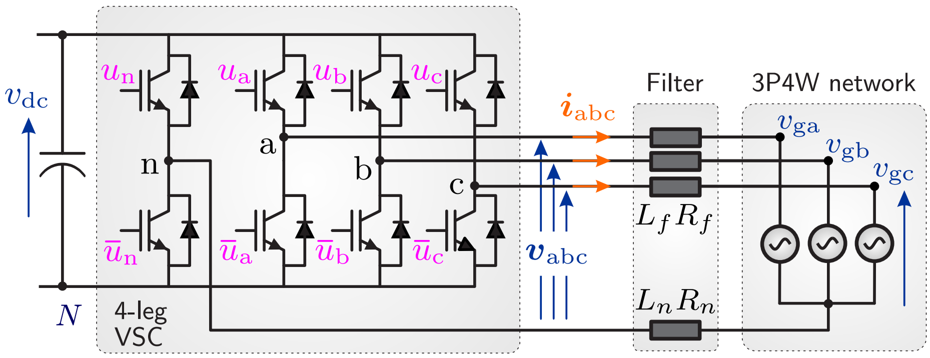

Figure 1.2: Grid-connected 4L-2L VSC.

1.1 State of art of Model Predictive Control

The main characteristic of predictive control is the use of a model of the system for predicting the future behavior of the controlled variables. This information is used by the controller to obtain the optimal actuation, according to a predefined optimization criterion. This structure has several important advantages [18]:

- Concepts are very intuitive and easy to understand.
- The multivariable case can be easily considered.

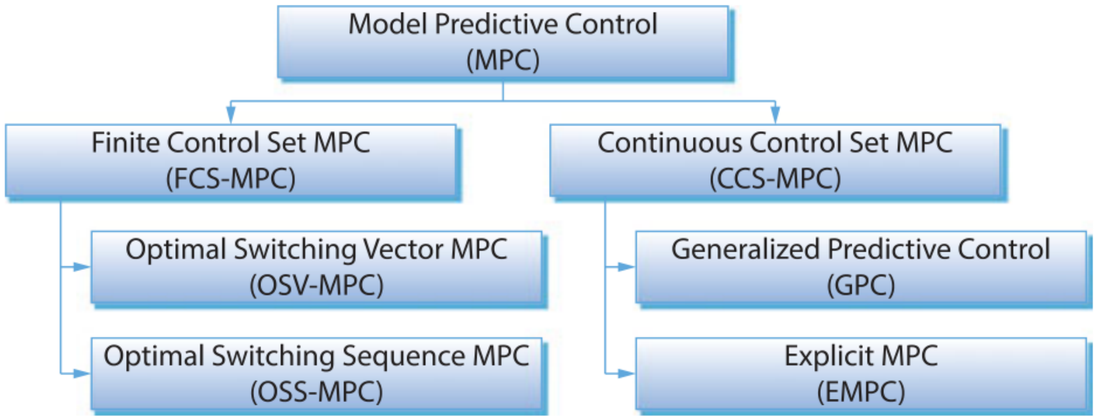

Figure 1.3: Classification of MPC strategies applied to power converters and drives. Figure taken from [1]

- Easy inclusion of non linearities in the model.
- Simple treatment of constraints and suitable for inclusion of modifications.
- The resulting controller is easy to implement.

Nevertheless, MPC presents some disadvantages:

- High computational cost.
- Highly sensitive to parameter variations.

If the system parameters change over time, estimation algorithms that consider these changes must be adapted or generated.

The MPC methods are classified based on the type of the optimization problem [24]. Fig. 1.3 shows the two principle classifications for MPC. On one hand, continuous control set MPC (CCS-MPC) computes a continuous control signal and then uses a modulator to synthesize the desired output voltage in the power converter. The main advantage of CCS-MPC is that it produces a fixed switching frequency due to the modulation stage. On the other hand, finite control set MPC (FCS-MPC) takes into account the discrete nature of the power converter to formulate the MPC algorithm and does not require an external modulator.

1.1.1 Basic principles of MPC

As previously mentioned MPC is a family of controllers that explicitly uses the model of the system to be controlled [1]. In general, MPC defines the control action by minimizing a cost function that describes the desired system behavior. This cost function compares the predicted system output with a reference where the predicted outputs are computed from the system model.

To illustrate the use of MPC for power electronics, a basic MPC strategy with a prediction horizon equal to one, applied to the current control of a voltage source inverter (VSI) with output RL load, is shown. The basic block diagram of this control strategy is presented in Fig. 1.4 , where the reference and predicted currents at instant k + 2 are used in order to compensate for the digital implementation delay [25].

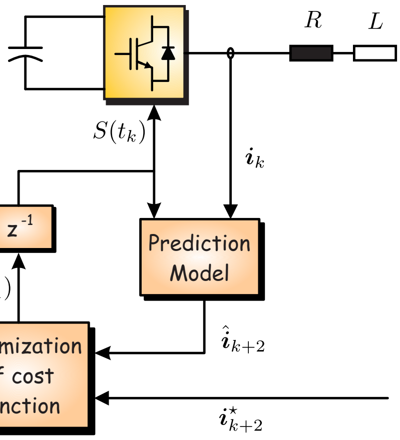

Figure 1.4: General scheme of basic MPC.

The algorithm is repeated for every switching period performing the following steps:

1. Optimal control action ($S(t_k)$) computed at instant t_{k-1} is applied to the converter.
2. Current $\boldsymbol{i}_k$ is measured at instant k. Also, the current reference $\boldsymbol{i}^\star_{k+2}$ is computed for instant $k+2$.
3. The predicted current $\hat{\boldsymbol{i}}_{k+2}$ is obtained through the system model.
4. Cost function is evaluated using $\boldsymbol{i}^\star_{k+2}$ and $\hat{\boldsymbol{i}}_{k+2}$. The optimal solution is determined by chosen the optimal control action ($S(t_k)$) that minimizes the function cost.

1.1.2 Continuous Control Set MPC

When a modulation stage is added to the control scheme the outputs of the controller are the duty cycles $d_i \in [0, 1]$. Thus, the decision variables of the optimal problem are continuous, typically resulting in a quadratic program (QP) [18].

CCS-MPC normally uses the discrete state-space model of the system define as:

$$\boldsymbol{x}(k+1) = A\boldsymbol{x}(k) + B\boldsymbol{u}(k) \tag{1.1}$$

with $\boldsymbol{u}(k) \in \Re^n$. Also, the cost function is usually defined as the error tracking of the state variables:

$$J(k) = ||\boldsymbol{x}^\star(k) - \boldsymbol{x}(k+1)||^2 \tag{1.2}$$

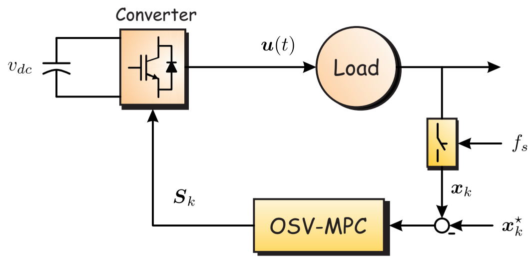

(a) OSV scheme.

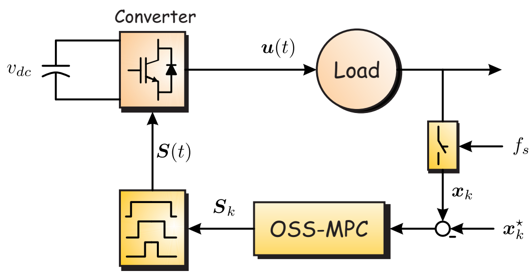

(b) OSS scheme

Therefore, the optimal calculation vector can be easily obtain by solving $\nabla g = 0$. The main disadvantage of this method is that the performance of the controller would be deteriorated by the parameter variations and nonlinearity [26].

1.1.3 Finite Control Set MPC

The main difference of FCS-MPC in contrast with the CCS-MPC is that the optimal solution lies within a limited set of options. In consequence, the optimal problem is transformed into an enumerated search algorithm where the prediction variables and the cost function (J) are evaluated for all feasible inputs of the system. In this case, where a power converter is utilized the cost function should be evaluated for all possible voltage output vectors of the inverter. The prediction model is defined just like in (1.1) but in this case the input of the system is $\boldsymbol{u}(k) \in \{\boldsymbol{u}_1, \boldsymbol{u}_2, ..., \boldsymbol{u}_n\}$ where n is an integer value and it is equal to the total number of switching states of the power converter.This class of MPC can be divided in the two following types:

1.1.3.1 Optimal Switching Vector MPC

The Optimal Switching Vector MPC (OSV-MPC) only synthesize one voltage vector in a complete switching period (Fig. 1.5a presents a diagram of this method). Consequently, no modulation stage is required. However, this method could lead to apply the same voltage vector in several consecutive switching cycles, causing a variable switching frequency in the system, producing a dispersed harmonic spectrum and higher ripple in the waveforms synthesize by the converter. Therefore, the use of this method of FCS-MPC is not recommended for grid connected power converter applications, due to the harmonic constraints imposed by the grid codes [2]. Moreover, OSV-MPC controller produces a nonzero average steady-state tracking error [27, 28]. This disadvantage becomes relevant when the variable to be controlled is the active power to be injected into the grid.

1.1.3.2 Optimal Switching Sequence MPC

Optimal Switching Sequence MPC (OSS-MPC) solves the harmonic spectrum problem caused in OSV-MPC considering a switching sequence instead of only one vector voltage in a switching period (Fig. 1.5b presents a diagram of this method). Because of this new consideration the OSS-MPC takes more computational burden since it adds the time application of the voltage vectors into the optimization problem.

Thus, the optimal control problem considers the instants where one switching vector changes from one state to another, which is essentially what a modulator does. In consequence, a suitable modulation scheme is typically integrated into the OSS-MPC strategy to emulate the desired switching sequence easily.

1.2 Objectives

1.2.1 Main Objective

To design and implement a predictive control scheme with vector modulation for a 4L-2L converter showing the potential of working as an active current filter.

1.2.2 Specific Objectives

- Review the current literature of MPC, characterize how the four-leg converter works, and search the regulatory requirements in the electrical standards on the harmonic content in distribution networks.
- Propose a predictive control strategy for a four-leg converter connected to the network to enhance the harmonic distortion obtained with the proposed strategy.
- Validate its performance through simulations analyzing its performance and comparing it with the traditional resonant controller.
- Implement a laboratory setup to test the performance of the proposed control strategy.

1.3 Work Methodology

This thesis work can be divided into four stages, where each one is strictly related to the objectives initially set.

The first two stages corresponds to the theoretical work (collection and modeling of the system), where the existing bibliography of the different predictive control strategies for three-leg converters should be reviewed and their operation and extrapolate it to a four-leg converter. For this, a bibliographical review of the switching states of the four-legged converters and their representation in the $\alpha\beta\gamma$ plane will be carried out, identifying the tetrahedrons that are generated and thus being able to mathematically formulate the appropriate predictive control scheme for this topology.

The third stage consist of running simulations using the software Matlab and Plecs that will be carried out to validate the results obtained with in the next stage in the laboratory setup. Also comparisons with traditional proportional-resonant controller will be carried out to demonstrate the merits of the proposed method. In this context, the response to reference changes and disturbances at the input of the system is compared.

The last stage of the work considers carrying out an experimental work, which will consist of starting up the four-leg converter connected to the network with an inductive filter between the grid and the converter, using the control strategy developed in the first and second stage. For this several test should be run to check that all the equipment used is properly calibrated. First, all current and voltage sensors should be calibrated for the range or current and voltage that will be used in the following laboratory experiments. Secondly, the dead time of each leg of the converter needs to be properly set. For this, an oscilloscope is used to check that there exist a adequate dead time to ensure that no short circuit occurs in the DC-link. Following, an open-loop test will be carried to confirm that modulation stage is well-function. A passive load is connected to the output of the 4L-2L converter to verify that sinusoidal currents are generated at the output of the system. All the tests mentioned at this point will not be presented at this work as they are considered routine test to make sure that the experimental setup is functional for the tests that will be carried out during this work. Finally, stationary state and dynamic tests will be performed to show up the good performance of the proposed strategy at different switching frequencies and in current references of different frequencies, demonstrating the benefits of using this kind of converter with this strategy as an active filter of harmonic and zero-sequence currents.

Chapter 2

Background theory

2.1 Grid-Connected Power Converters

Power converters play an important role in DG and RE generation. They are also widely used in industrial applications such as energy storage systems, active-front-end rectifiers and power conditioning units [29].

Power converters are autonomous equipment, and therefore their performance does not only depend on the equipment design (topology) but also on the control strategy used. The following list enumerates the main operating requirements of a drive, not only related to the closed-loop response but also to the safe operation of the drive and the load (or network):

- Fixed or limited switching frequency: the importance of this characteristic is reflected in two points. On one hand, the switching frequency is related to the losses of the converter, which must be taken into account when designing the equipment in terms of efficiency and thermal dissipation. On the other hand, it directly determines the harmonic spectrum at the converter output, facilitating the design of the filters used.

- Reduced ripple: This helps to reduce the dimension of the passive elements in the converter (capacitors and inductors).

- Fast dynamic response: Converters are often part of larger systems, where fast power flow changes are required. Therefore a fast dynamic response is needed to fulfill this need.

- Steady-state zero error: Standard controllers are designed to follow constant references. However, in alternating current systems, sinusoidal references must be followed. If the current or voltage do not have the stipulated amplitude or phase, undesired effects could occur. For example, if a converter wants to work with unity power factor, this type of error could cause reactive power to be injected or delivered by the converter.

- Reduced harmonic content: in AC systems it is required that the current and voltage present only a fundamental frequency signal and in DC systems they must present continuous signals. If the harmonic content is too high, it can lead to unwanted effects. For example, in electrical drives, increased losses can be generated in the electrical machine. In applications where the converter is connected to the network, resonances can occur in the system.

Some of these requirements contradict others, for example a fast dynamic response with low harmonic content. This dependency is of high importance when selecting the control method that effectively meets all or almost all of the aforementioned requirements.

In the last decade, DC/AC power converters (inverters) have been widely used in RE applications as grid interfaces. In wind turbines and photovoltaic systems, inverters are used to connect the generation system to the grid and extract energy from the renewable source to transfer it to the electrical system. In other words, the main objective of the inverter is to control the power delivered to the system, complying with the necessary quality requirements. An additional functionality of this type of converter is that it is possible to control the reactive power delivered or absorbed, without compromising the active power delivered to the grid.

In wind generation systems, the transformation of energy from wind to electricity is done directly in AC, therefore, to connect the generator to the inverter, an AC/DC converter (rectifier) is typically used. This together with the inverter make up the system known as Back-to-Back (BTB). On the other hand, in photovoltaic systems, the transformation of energy occurs in DC, so a DC/DC converter is used to connect the generation to the inverter.

Due to the reasons mentioned above, the inverter is of special interest since it is a common factor in the applications that can be given to converters today. One of the main uses for this kind of converter is the shunt active filter [30]. The main task of this configuration is to deliver through the inverter all the harmonic currents in the system generated by nonlinear loads reducing the harmonic distortion in the grid allowing to fulfill regulatory requirements. Fig. 2.1 shows a basic diagram of the shunt active filter. The active filter controller can be divided into two parts:

- Current reference generator: The active filter controller is a closed-loop current controller. It needs to continuously sense the load current i_L to compute the instantaneous values of the compensating current reference $i_C^\star$ that will be send to the current controller

- Current controller: Is the part of the controller in charge of synthesize the compensating current calculated by the current reference generator.

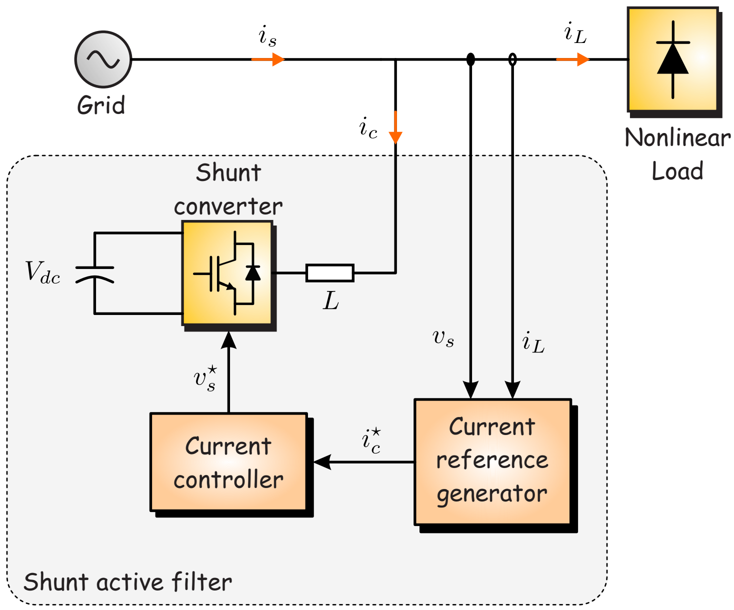

Figure 2.1: Basic interface of shunt active filter.

The shunt converter needs to work with a high switching frequency f_s in order to reproduce accurately the compensation currents. Normally, $f_s > 10f_{h_{max}}$, where $f_{h_{max}}$ represents the frequency of the highest order of harmonic current that is going to be compensated.

In Fig.2.1 a voltage-source converter (VSC) is used to represent the shunt converter since almost all shunt active filter in commercial operation use this kind of converter [31]. It can be seen in the figure that the number of wires of the system is not specified. The reason for this is that the power system can be a three-phase three-wire (3P3W) system or a three-phase-four-wire (3P4W) system, the only difference is that the second option considers the neutral wire adding a zero-sequence current to the network. Thus, depending on the characteristics of the system the VSC could be a three-leg o a four-leg converter, so that it can compensate zero-sequence component in addition to harmonic currents if needed [11]. Therefore, the active filter is also capable of compensating reactive current. In this way, the network is only responsible for delivering the active component of the current while any other component will be delivered by the active current filter.

2.2 Current Harmonic Requirements

The integration of renewable sources into the electrical system has been motivated by environmental problems and political and economic incentives. However, this fact has meant a technical and technological challenge with respect to reliability, stability and power quality of the system. Under this perspective, the impact of the converters connected to the network becomes more significant.

The requirements regarding power quality are mainly focused on maintaining the quality of the network voltage in amplitude, frequency and phase. A voltage disturbance is mainly due to power disturbances (due to the random behavior of some generation sources) or due to transient operations in the system (such as the switching on of high-power induction motors). However, the quality of the current injected into the network is also relevant, and in this sense, the converters connected to the network are responsible for complying with the quality standards imposed by the international [2] and local standards.

The current injected into the network must not have a total harmonic distortion greater than 5%. The Total Demanded Distortion (TDD) is defined as:

$$I_{TDD} = \frac{1}{\sqrt{2}I_{nom}} \sqrt{\sum_{h\neq 1} I_{g,h}^2} \tag{2.1}$$

where I_{nom} corresponds to the rated current of the system and $I_{g,h}$ with $h > 1$ corresponds to the harmonic currents of frequency hf_1. In a three-phase system, the TDD is calculated for each phase and then the values obtained are averaged.

Maximum harmonic current distortion in percent of I_L						
Individual odd harmonic order (odd harmonics)						
I_{sc}/I_L	$2 \leq h < 11$	$11 \leq h < 17$	$17 \leq h < 23$	$23 \leq h < 35$	$35 \leq h < 50$	TDD
< 50	4.0	2.0	1.5	0.6	0.3	5.0
$20 < 50$	7.0	3.5	2.5	1.0	0.5	8.0
$50 < 100$	10.0	4.5	4.0	1.5	0.7	12.0
$100 < 1000$	12.0	5.5	5.0	2.0	1.0	15.0
> 1000	15.0	7.0	6.0	2.5	1.4	20.0

Table 2.1: Table extracted from [2]. Shows the harmonic content limit accepted by the standard for voltage systems between 120 [V] and 69 [kV]

2.3 Description of the 4L-2L VSC

The circuit diagram of a 4L-2L VSC connected to a 3P4W network through an L-filter is shown in Fig. 1.2. The converter comprises 2 switches in each leg, producing a total of $2^4 = 16$ switching positions $\boldsymbol{u}_{\text{abcn}} \in \{0, 1\}^4$, which are listed in table 2.2. Accordingly, the three-phase output voltage vector can be defined in terms of these switching positions as:

$$\boldsymbol{v}_{\text{abc}} = v_{\text{dc}} \underbrace{\left[u_{\text{a}} - u_{\text{n}}, u_{\text{b}} - u_{\text{n}}, u_{\text{c}} - u_{\text{n}}\right]^\top}_{u_{\text{abc}}} \tag{2.2}$$

where $\boldsymbol{u}_{\text{abc}}$ is the three-phase switching state of the converter. Using the amplitude invariant Clarke transform $\mathbf{T}_{\alpha\beta\gamma}$ [30], it is possible to represent $\boldsymbol{u}_{\text{abc}}$ in the $\alpha\beta\gamma$ frame-

Table 2.2: Switching states of a 4L-2L converter. Voltage values normalized by V_{dc}.

States $[S_a,S_b,S_c,S_n]$	Vectors	u_{an}	u_{bn}	u_{cn}	u_α	u_β	u_0
0000	$\boldsymbol{u}_{s_0}$	0	0	0	0	0	0
0001	$\boldsymbol{u}_{s_1}$	-1	-1	-1	0	0	-1
0010	$\boldsymbol{u}_{s_2}$	0	0	1	$-1/3$	$-\sqrt{3}/3$	$1/3$
0011	$\boldsymbol{u}_{s_3}$	-1	-1	0	$-1/3$	$-\sqrt{3}/3$	$-2/3$
0100	$\boldsymbol{u}_{s_4}$	0	1	0	$-1/3$	$\sqrt{3}/3$	$1/3$
0101	$\boldsymbol{u}_{s_5}$	-1	0	-1	$-1/3$	$\sqrt{3}/3$	$-2/3$
0110	$\boldsymbol{u}_{s_6}$	0	1	1	$-2/3$	0	$2/3$
0111	$\boldsymbol{u}_{s_7}$	-1	0	0	$-2/3$	0	$-1/3$
1000	$\boldsymbol{u}_{s_8}$	1	0	0	$2/3$	0	$1/3$
1001	$\boldsymbol{u}_{s_9}$	0	-1	-1	$2/3$	0	$-2/3$
1010	$\boldsymbol{u}_{s_{10}}$	1	0	1	$1/3$	$-\sqrt{3}/3$	$2/3$
1011	$\boldsymbol{u}_{s_{11}}$	0	-1	0	$1/3$	$-\sqrt{3}/3$	$-1/3$
1100	$\boldsymbol{u}_{s_{12}}$	1	1	0	$1/3$	$\sqrt{3}/3$	$2/3$
1101	$\boldsymbol{u}_{s_{13}}$	0	0	-1	$1/3$	$\sqrt{3}/3$	$-1/3$
1110	$\boldsymbol{u}_{s_{14}}$	1	1	1	0	0	1
1111	$\boldsymbol{u}_{s_{15}}$	0	0	0	0	0	0

work as:

$$\boldsymbol{u}_{\mathrm{s}} = \left[\begin{array}{ccc} u_{\mathrm{s}}^{\alpha} & u_{\mathrm{s}}^{\beta} & u_{\mathrm{s}}^{\gamma} \end{array}\right]^{\top} = \mathbf{T}_{\alpha\beta\gamma}\boldsymbol{u}_{\mathrm{abc}} \in \mathbb{V} \tag{2.3}$$

Thus, the voltage vector in $\alpha\beta\gamma$ coordinates is $\boldsymbol{v}_{\mathrm{s}} = v_{\mathrm{dc}}\boldsymbol{u}_{\mathrm{s}}$. Fig. 2.2 shows the three-dimensional representation of the 16 switching states in the $\alpha\beta\gamma$ space. Therein, $\boldsymbol{u}_{\mathrm{s}0}$ is the zero vector with single redundancy, and vectors $\boldsymbol{u}_{\mathrm{s}1}$ to $\boldsymbol{u}_{\mathrm{s}14}$ are the active switching vectors. The space formed by these vectors, highlighted in gray color in Fig. 2.2, represents the control region of the 4L-2L VSC.

Fig. 2.3(a) shows a top view of the control region depicted in Fig. 2.2. Like conventional 3-leg 2-level VSCs, the modulation region in $\alpha\beta$ space corresponds to a hexagon comprised of six sectors $\mathcal{S}_\ell$ with $\ell \in \{1, \ldots, 6\}$. However, in the case of 4L-2L VSCs, each sector can be extended over the γ axis generating a pentahedron. For instance, Fig. 2.3(b) shows the pentahedron formed along with sector $\mathcal{S}_2$. Each pentahedron comprises six active vectors and the zero-vector, creating 4 tetrahedra and leading to 24 tetrahedra in the complete region shown in Fig. 2.2. In turns, each tetrahedron is formed by the zero-vector and three active vectors, defining the smallest region where a reference vector can be enclosed. Thereby, in this work, each of the 24 tetrahedra is denoted as: $\mathcal{T}_j(x, y, x)$, where $j \in \mathcal{R} = \{1, \ldots 24\}$, and $\{x, y, x\} \in \Upsilon = \{1, \ldots, 14\}$ indicates the active switching vectors comprising the jth tetrahedron. In this work, the tetrahedra are sequentially enumerated from the bottom to the top of pentahedron $\mathcal{S}_\ell$ as $j = 4(\ell - 1) + \kappa$, where $\kappa \in \{1, \ldots, 4\}$.

To synthesize a desired output voltage, the four nearest switching vectors are com-

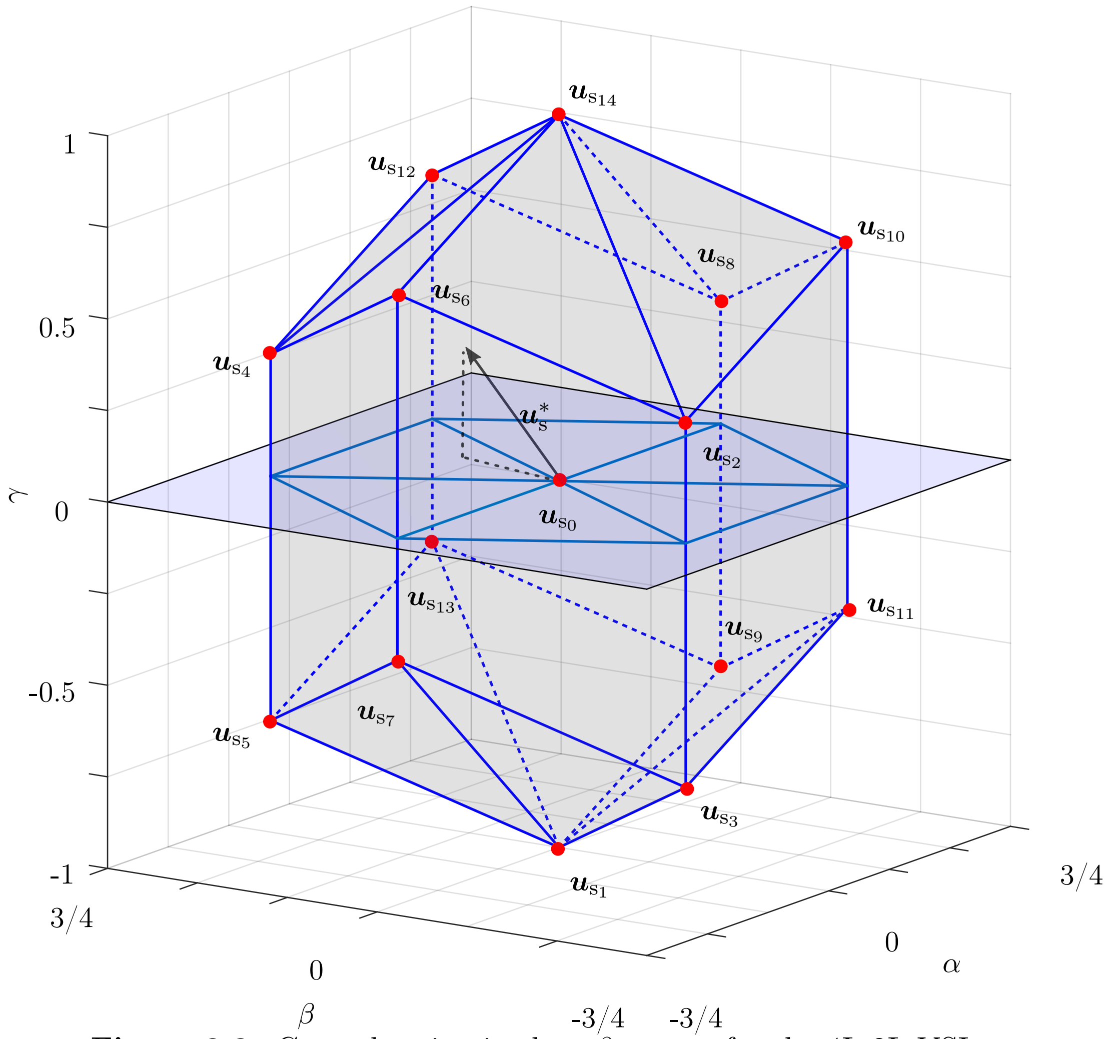

Figure 2.2: Control region in the $\alpha\beta\gamma$ space for the 4L-2L-VSI.

monly employed in carrier-based and space vector PWM techniques for 4-leg inverter, which are arranged in a specific switching sequence [32]. Discontinuous seven-segment switching sequence (7S-SS), using only one redundancy of the zero vector (either $\boldsymbol{u}_{\mathrm{s0N}}$ or $\boldsymbol{u}_{\mathrm{s0P}}$), can be implemented to reduce switching frequency at the cost of more harmonic distortion. Symmetrical nine-segment switching sequences 9S-SS can be also implemented using both redundancies of the zero vector, improving the harmonic spectrum of the synthesized waveforms, at the cost of higher switching commutation. Fig. 3.1 shows the symmetrical 9S-SS for tetrahedron $\mathcal{T}_7(4, 12, 13)$.

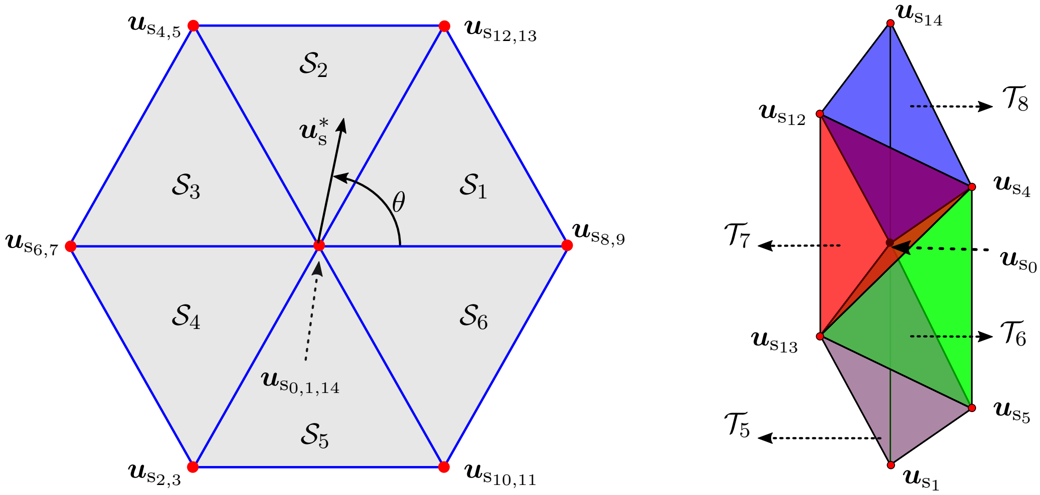

Figure 2.3: (a) Top view of the control region of the 4L-2L-VSI over the $\alpha\beta$ -plane. (b) The four tetrahedra that form the extension of sector $\mathcal{S}_2$ over γ axis (tetrahedron $\mathcal{T}_5$ to $\mathcal{T}_8$)

Chapter 3

Proposed Optimal Switching Sequence MPC Strategy

In this chapter the proposed OSS-MPC strategy will be formulated. To do this several steps will be followed. First, the continuous-time model of the system is obtained. After this, the discrete model is achieved in order to obtain the model prediction of the system. Next, the cost function is formulated. This will allow to obtain the equations to compute the duty cycles or time application of the vectors. Also, an algorithm is shown to calculate the duty cycles in cases of over-modulation. After this, the algorithm to define the optimal solution is defined, proposing a method that will reduce the computational burden. Then, is a section explaining the tuning of the controller and how it is manipulated to change the dynamics of the system. Afterwards, it is explained how the modulating signals (that will be compared with the carrier signal) are computed. Finally, some tools that where used to achieve a better performance of the proposed method are presented and explained (Kalman filter and compensation of future references).

3.1 OSS-MPC for 4-Leg Grid-Tied Converters

3.1.1 Discrete-Time Model: The Average Trajectory

To formulate the control strategy, the continuous-time model of the system shown in Fig. 1.2 is expressed in $\alpha\beta\gamma$ coordinates as:

$$\frac{\mathrm{d}\boldsymbol{i}_{\mathrm{g}}}{\mathrm{d}t} = -\mathbf{L}^{-1}\mathbf{R}\boldsymbol{i}_{\mathrm{g}} - \mathbf{L}^{-1}\boldsymbol{v}_{\mathrm{g}} + \mathbf{L}^{-1}v_{\mathrm{dc}}\boldsymbol{u}_{\mathrm{s}} \tag{3.1}$$

where $\boldsymbol{i}_{\mathrm{g}} = \begin{bmatrix} i_{\mathrm{g}}^{\alpha} & i_{\mathrm{g}}^{\beta} & i_{\mathrm{g}}^{\gamma} \end{bmatrix}^{\intercal}$ and $\boldsymbol{v}_{\mathrm{g}} = \begin{bmatrix} v_{\mathrm{g}}^{\alpha} & v_{\mathrm{g}}^{\beta} & v_{\mathrm{g}}^{\gamma} \end{bmatrix}^{\intercal}$ are the grid current and voltage vectors, respectively. In (3.1), the matrices are defined as:

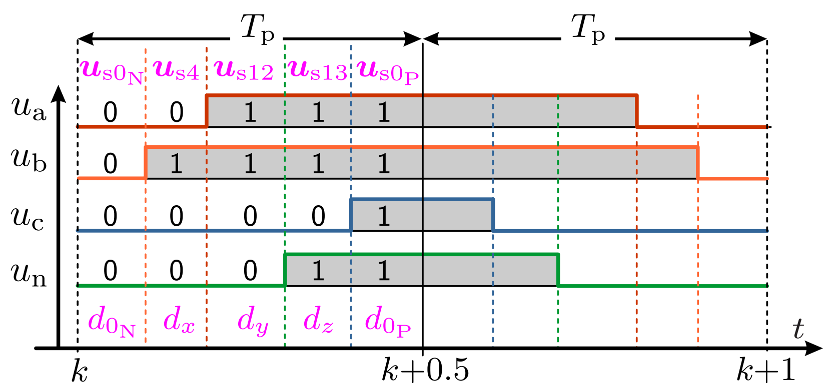

Figure 3.1: Symmetrical 9S-SS for the tetrahedron $\mathcal{T}_7(4, 12, 13)$.

$$\mathbf{L} = \begin{bmatrix} L_f & 0 & 0 \\ 0 & L_f & 0 \\ 0 & 0 & L_\gamma \end{bmatrix} \quad \mathbf{R} = \begin{bmatrix} R_f & 0 & 0 \\ 0 & R_f & 0 \\ 0 & 0 & R_\gamma \end{bmatrix} \tag{3.2}$$

being L_γ=L_f+3L_n and R_γ=R_f+3R_n, the zero-sequence inductance and resistance, respectively.

Typically in FCS-MPC strategies applied to 4-leg inverters [9, 11, 21, 22], the optimal switching action is obtained from minimizing a cost function capturing the instantaneous tracking error of the grid currents along with the switching effort (to control the switching frequency indirectly). Consequently, the closed-loop performance depends on the weighting factor choice, which is not trivial to perform [33, 34]. This work proposes tracking the average trajectory of the grid currents (over the switching cycle T_s) by adequately manipulating the application times of the switching vectors comprised in the 9S-SS. Thus, the average tracking error is improved by the proposed controller. Moreover, the subsequent modulation stage, used to synthesize the desired switching sequence, fixes the switching frequency, avoiding the use of a weighting factor and resulting in deterministic switching losses.

For modeling the grid current average trajectory over one switching period T_s, two assumptions are made. First, the interval T_s is much lesser than the shortest time constant of the system, i.e., $T_s \ll L_f/R_f$. Accordingly, when the converter applies a given 9S-SS, the grid current $\boldsymbol{i}_g(t)$ evolves linearly over each subinterval t_i. Hence, the trajectory can be considered as a piecewise linear function of the time, as illustrated in Fig. 3.2. Thus, the instantaneous evolution of $\boldsymbol{i}_\mathrm{g}$ can be sequentially computed by employing the Forward Euler method as

$$\boldsymbol{i}_{\mathrm{g}(i+1)} = \boldsymbol{i}_{\mathrm{g}(i)} + \left.\frac{\mathrm{d}\boldsymbol{i}_\mathrm{g}}{\mathrm{d}t}\right|_i T_\mathrm{p} d_i \tag{3.3}$$

where $d_i = t_i/T_\mathrm{p} \in \mathbb{D} \triangleq [0,\, 1]$ is the normalized application time (duty cycle), and T_p=$T_\mathrm{s}/2$ is the sub-cycle period. Besides, due to the symmetrical nature of the 9S-SS, the average trajectory of $\boldsymbol{i}_\mathrm{g}$ is equal to its value at the end of the sub-cycle ($\boldsymbol{i}_{\mathrm{g}5}$ in

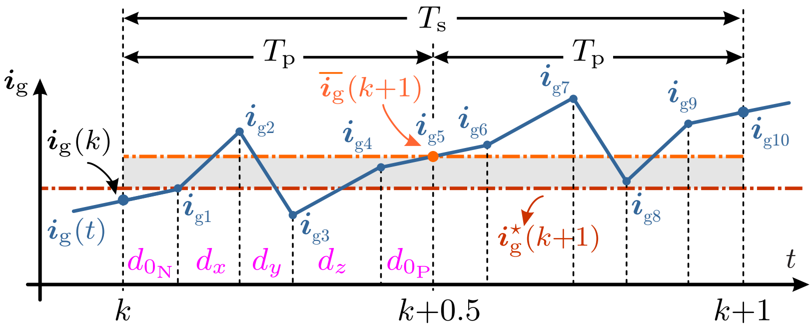

Figure 3.2: Predicted system trajectory for a 9S-SS.

Fig. 3.2). Thus, it is expressed as:

$$\overline{\boldsymbol{i}_{\mathrm{g}}}(k+1) = \boldsymbol{i}_{\mathrm{g}}(k) + \sum_{i\in\mathcal{I}} \left.\frac{\mathrm{d}\boldsymbol{i}_{\mathrm{g}}}{\mathrm{d}t}\right|_{i}, \quad \mathcal{I} = \{0_{\mathrm{N}}, x, y, z, 0_{\mathrm{P}}\} \tag{3.4}$$

Second, it is assumed that the fundamental period of the grid voltages is much higher than T_{p}. Then, every sub-interval gradient, i.e., $\left.\frac{\mathrm{d}\boldsymbol{i}_g}{\mathrm{d}t}\right|_i$, is computed using the system variables sampled values at instant k. Accordingly, by introducing the duty cycle vector $\boldsymbol{d}(k)$ and switching matrix $\boldsymbol{U}(k)$ defined as:

$$\boldsymbol{d}(k) \triangleq \begin{bmatrix} d_0(k) & d_x(k) & d_y(k) & d_z(k) \end{bmatrix}^{\intercal} \in \mathbb{D}^4, \tag{3.5}$$

$$\boldsymbol{U}(k) \triangleq \begin{bmatrix} \boldsymbol{u}_{\mathrm{s}0}(k) & \boldsymbol{u}_{\mathrm{s}x}(k) & \boldsymbol{u}_{\mathrm{s}y}(k) & \boldsymbol{u}_{\mathrm{s}z}(k) \end{bmatrix}, \tag{3.6}$$

the average trajectory (3.4) can be expressed as:

$$\overline{\boldsymbol{i}_{\mathrm{g}}}(k+1) = \mathbf{A}\boldsymbol{i}_{\mathrm{g}}(k) + \mathbf{P}\boldsymbol{v}_{\mathrm{g}}(k) + \mathbf{B}\boldsymbol{U}(k)\boldsymbol{d}(k) \tag{3.7}$$

with $\mathbf{A} = (\mathbf{I} - \mathbf{L}^{-1}\mathbf{R}T_{\mathrm{p}})$, $\mathbf{P} = -T_{\mathrm{p}}\mathbf{L}^{-1}$, $\mathbf{B} = v_{\mathrm{dc}}T_{\mathrm{p}}\mathbf{L}^{-1}$, $d_0 \triangleq d_{0_{\mathrm{P}}} + d_{0_{\mathrm{N}}}$ and $\boldsymbol{u}_0 \triangleq \boldsymbol{u}_{\mathrm{s}0_{\mathrm{P}}} = \boldsymbol{u}_{\mathrm{s}0_{\mathrm{N}}}$.

Unlike the OSS-MPC strategies for 3-leg VSCs (e.g., [35] [36] [37]), the duty cycle vector $\boldsymbol{d}$ has four components and every switching sequence is defined by 4 switching vectors in matrix $\boldsymbol{U}$. Hence, the average switching vector applied by the converter is given by $\boldsymbol{u}(k) = \boldsymbol{U}(k)\boldsymbol{d}(k)$.

For the sake of simplicity, hereinafter $\overline{\boldsymbol{i}_{\mathrm{g}}}(k+1)$ will be denoted as $\boldsymbol{i}_{\mathrm{g}}(k+1)$; and therefore, (3.7) will be considered as the discrete-time model.

3.1.2 Optimal Control Problem

To obtain the optimal duty cycles for every switching sequence candidate $\boldsymbol{S}_j(\boldsymbol{U}_j, \boldsymbol{d}_j)$, the following objective function is introduced

$$J_j = \left\|\boldsymbol{i}_{\mathrm{g}}(k+1) - \boldsymbol{i}_{\mathrm{g}}^{*}(k+1)\right\|_2^2 + \left\|\boldsymbol{\Lambda}_u \left(\boldsymbol{U}_j \boldsymbol{d}_j - \boldsymbol{u}_{\mathrm{ss}}(k)\right)\right\|_2^2, \tag{3.8}$$

This quadratic cost function is formulated to quantify two control objectives: the average tracking error and the control effort. The diagonal matrix $\boldsymbol{\Lambda}_u = \mathrm{diag}(\lambda_u^{\alpha}, \lambda_u^{\beta}, \lambda_u^{\gamma})$ is used to adjust the compromise between both control objectives, avoiding the proposed OSS-MPC behaving like a deadbeat controller because this may produce robustness issues [18].

Indeed, by substituting (3.7) into (3.8), the cost function can be rewritten in the following equivalent form:

$$J_j = \left\|\mathbf{B}\left(\boldsymbol{U}_j \boldsymbol{d}_j - \boldsymbol{u}_{\mathrm{db}}(k)\right)\right\|_2^2 + \left\|\boldsymbol{\Lambda}_u \left(\boldsymbol{U}_j \boldsymbol{d}_j - \boldsymbol{u}_{\mathrm{ss}}(k)\right)\right\|_2^2, \tag{3.9}$$

where $\boldsymbol{u}_{\mathrm{db}}(k)$ is the deadbeat control input defined as

$$\boldsymbol{u}_{\mathrm{db}}(k) = \mathbf{B}^{-1}\left(\boldsymbol{i}_{\mathrm{g}}^{\star}(k+1) - \mathbf{A}\boldsymbol{i}_{\mathrm{g}}(k) - \mathbf{P}\boldsymbol{v}_{\mathrm{g}}(k)\right) \tag{3.10}$$

Moreover, in the second term of (3.9), the signal $\boldsymbol{u}_{\mathrm{ss}}(k)$ is the control input that ensures the output currents track their references under ideal conditions in which both the disturbances and system parameters are certainly known [18, 35]. Thus, $\boldsymbol{u}_{\mathrm{ss}}(k)$ refers to open-loop or steady-state control input, and it is determined from (3.1) as:

$$\boldsymbol{u}_{\mathrm{ss}}(k) = \frac{1}{v_{\mathrm{dc}}(k)}\left(\mathbf{L}\frac{\mathrm{d}\boldsymbol{i}_{\mathrm{g}}^{*}(k)}{\mathrm{d}t} + \mathbf{R}\boldsymbol{i}_{\mathrm{g}}^{*}(k) + \boldsymbol{v}_{\mathrm{g}}(k)\right) \tag{3.11}$$

Therefore, by inspecting (3.9), it is shown that the positive definite matrix $\boldsymbol{\Lambda}_u$ allows the dynamic response and the robustness properties of the closed-loop system to be modified [28]. Further details on the methodology used to design the parameters of the tuning matrix $\boldsymbol{\Lambda}_u$ will be presented in section 3.1.5.

On the other hand, as described in (3.9), for every tetrahedron $j \in \mathcal{R}$, the cost

$$\Theta_j = u_{xj}^{\alpha}u_{yj}^{\gamma}u_{zj}^{\beta} - u_{xj}^{\alpha}u_{yj}^{\beta}u_{zj}^{\gamma} + u_{xj}^{\beta}u_{yj}^{\alpha}u_{zj}^{\gamma} - u_{xj}^{\beta}u_{yj}^{\gamma}u_{zj}^{\alpha} - u_{xj}^{\gamma}u_{yj}^{\alpha}u_{zj}^{\beta} + u_{xj}^{\gamma}u_{yj}^{\beta}u_{zj}^{\alpha} \tag{3.18a}$$

$$d_{\mathrm{r}xj} = \frac{1}{\Theta_j}\Big(u_{\mathrm{uc}}^{\alpha}(u_{yj}^{\gamma}u_{zj}^{\beta} - u_{yj}^{\beta}u_{zj}^{\gamma}) + u_{\mathrm{uc}}^{\beta}(u_{yj}^{\alpha}u_{zj}^{\gamma} - u_{yj}^{\gamma}u_{zj}^{\alpha}) + u_{\mathrm{uc}}^{\gamma}(u_{yj}^{\beta}u_{zj}^{\alpha} - u_{yj}^{\alpha}u_{zj}^{\beta})\Big) \tag{3.18b}$$

$$d_{\mathrm{r}yj} = \frac{1}{\Theta_j}\Big(u_{\mathrm{uc}}^{\alpha}(u_{xj}^{\beta}u_{zj}^{\gamma} - u_{xj}^{\gamma}u_{zj}^{\beta}) + u_{\mathrm{uc}}^{\beta}(u_{xj}^{\gamma}u_{zj}^{\alpha} - u_{xj}^{\alpha}u_{zj}^{\gamma}) + u_{\mathrm{uc}}^{\gamma}(u_{xj}^{\alpha}u_{zj}^{\beta} - u_{xj}^{\beta}u_{zj}^{\alpha})\Big) \tag{3.18c}$$

$$d_{\mathrm{r}zj} = \frac{1}{\Theta_j}\Big(u_{\mathrm{uc}}^{\alpha}(u_{xj}^{\gamma}u_{yj}^{\beta} - u_{xj}^{\beta}u_{yj}^{\gamma}) + u_{\mathrm{uc}}^{\beta}(u_{xj}^{\alpha}u_{yj}^{\gamma} - u_{xj}^{\gamma}u_{yj}^{\alpha}) + u_{\mathrm{uc}}^{\gamma}(u_{xj}^{\beta}u_{yj}^{\alpha} - u_{xj}^{\alpha}u_{yj}^{\beta})\Big) \tag{3.18d}$$

$$d_{\mathrm{r}0j} = 1 - d_{\mathrm{r}xj} - d_{\mathrm{r}yj} - d_{\mathrm{r}zj} \tag{3.18e}$$

function is expressed as a function of the matrix $\boldsymbol{U}_j$ and the normalized application times $\boldsymbol{d}_j$. Consequently, the OSS is obtained by solving, at each sampling period k, the following OSS-MPC problem [38]:

$$\boldsymbol{S}_{\text{op}} = \arg\min_{\boldsymbol{U}_j}\big\{ \min_{\boldsymbol{d}_j} J(\boldsymbol{d}_j, \boldsymbol{U}_j)\big\} \tag{3.14a}$$

$$\text{s.t.} \quad \mathbb{1}^\intercal \boldsymbol{d}_j = 1 \tag{3.14b}$$

$$\boldsymbol{d}_j \geq 0 \tag{3.14c}$$

It is worth highlighting that the optimal control problem underlying the OSS-MPC (3.14) considers two nested optimizations. First, in the internal optimization step, a local minimal solution $\boldsymbol{d}_j$ is obtained for the jth switching sequence candidate (where $j \in \mathcal{R}$). Then, in the external optimization stage, the pair $\{\boldsymbol{U}^\star,\ \boldsymbol{d}^\star\}$ providing the minimum cost function value defines the OSS, namely $\boldsymbol{S}_{\text{op}}$.

3.1.3 Duty Cycles Calculation

To solve the OSS-MPC problem (3.14), it is proposed first to compute the relaxed solution to the inner optimization stage. To this end, constraint $\boldsymbol{d}_j \geq 0$ is ignored, and thus, the relaxed solution, namely $\boldsymbol{d}_{\text{r}}$, is the one that solves the following bi-objective constrained least-square problem,

$$\begin{aligned} &\min_{\boldsymbol{d}_{\text{r}j}} \ \big\|\mathbf{B}(\boldsymbol{U}_j\boldsymbol{d}_{\text{r}j} - \boldsymbol{u}_{\text{db}})\big\|_2^2 + \big\|\boldsymbol{\Lambda}_u(\boldsymbol{U}_j\boldsymbol{d}_{\text{r}j} - \boldsymbol{u}_{\text{ss}})\big\|_2^2 \\ &\text{s.t.} \ \ \mathbb{1}^\intercal \boldsymbol{d}_{\text{r}j} = 1. \end{aligned} \tag{3.15}$$

Thereby, using the Lagrange multipliers, the solution to (3.15) for every switching sequence candidate is given by:

$$\boldsymbol{d}_{\text{r}j}(k) = \begin{bmatrix} \boldsymbol{U}_j \\ \mathbb{1}^\top \end{bmatrix}^{-1} \begin{bmatrix} \boldsymbol{u}_{\text{uc}}(k) \\ 1 \end{bmatrix} \tag{3.16}$$

where $\boldsymbol{u}_{\text{uc}}(k)$ is the unconstrained average switching vector (UASV) defined as:

$$\boldsymbol{u}_{\text{uc}}(k) = \left(\mathbf{B}^\top\mathbf{B} + \boldsymbol{\Lambda}_u^\top\boldsymbol{\Lambda}_u\right)^{-1}\left(\mathbf{B}^\top\mathbf{B}\boldsymbol{u}_{\text{db}}(k) + \boldsymbol{\Lambda}_u^\top\boldsymbol{\Lambda}_u\boldsymbol{u}_{\text{ss}}(k)\right) \tag{3.17}$$

Thus, by using (3.6) into (3.16), the relaxed solution associated with the jth switching sequence candidate is computed by using the closed-form solution in (3.18). Therein, only the $\alpha\beta\gamma$ components of both the UASV, $\boldsymbol{u}_{\text{uc}}(k)$, and the switching vectors comprising every switching sequence, $\{\boldsymbol{u}_{xj},\ \boldsymbol{u}_{yj},\ \boldsymbol{u}_{zj}\}$, are needed to calculate the relaxed duty cycles.

However, it is worth highlighting that the solution in (3.18) does not necessarily satisfy the non-negative constraint (3.14c). Thus, unfeasible solutions could be provided by the controller under some operating conditions. Specifically, during transients, the vector $\boldsymbol{u}_{\text{uc}}(k)$ could be fallen outside the control region shown in Fig. 2.2. On that condition, the application time for the null switching vectors must be negative

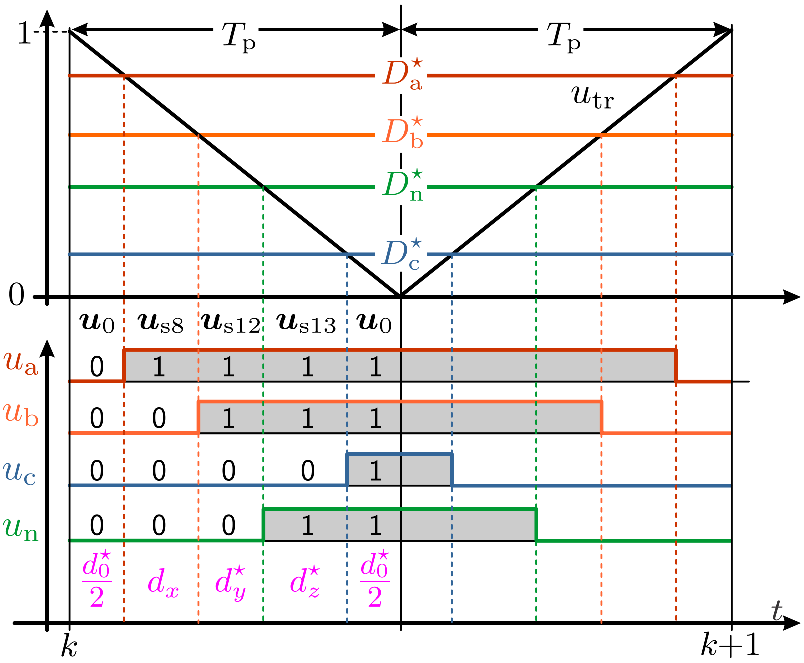

Figure 3.3: Single-carrier-based PWM to synthesize the desired SS.

($d_0 < 0$) to compensate for the over-application of the active switching vectors. To provide feasible solutions, the duty cycle vector is computed from the relaxed one $\boldsymbol{d}_{\mathrm{r}j}$ as:

$$\boldsymbol{d}_j = \frac{\boldsymbol{d}^+_{\mathrm{r}j}}{\mathbb{1}^\top \boldsymbol{d}^+_{\mathrm{r}j}} \tag{3.19}$$

where $\boldsymbol{d}^+_{\mathrm{r}j} = \max(0, \boldsymbol{d}_{\mathrm{r}j})$ leads to the non-negative values of $\boldsymbol{d}_{\mathrm{r}j}$. Notice that the relaxed solution given in (3.19) is the optimal application times under steady-state operation since $\boldsymbol{d}^+_{\mathrm{r}j} = \boldsymbol{d}_{\mathrm{r}j}$ and $\mathbb{1}^\top \boldsymbol{d}_{\mathrm{r}j} = 1$. However, depending on the closed-loop dynamic achieved by the proposed OSS-MPC, the controller can lead to suboptimal solutions during transients.

3.1.4 Cost function minimization and OSS selection

Since the controller can calculate the duty cycle vector for every switching sequence candidate using (3.18) and (3.19), the optimal one needs to be further selected to determine the OSS. If computationally feasible, this task can be done by exhaustively enumerating all candidate solutions using the same working principle of the standard FCS-MPC strategy (e.g., [36, 39]). It means that the cost function (3.9) must be computed for all switching sequence candidates $j \in \mathcal{R}$ using the duty cycles $\boldsymbol{d}_j$ firstly calculated from (3.18) and (3.19). Thus, the index with the minimal cost function value, namely j_op, defines the optimal switching sequence $\boldsymbol{S}_\mathrm{op} = \{\boldsymbol{d}^\star, \boldsymbol{U}^\star\}$.

Aiming to reduce the computational burden, in this work, the OSS-MPC algorithm introduced in [35] for 3L-NPC converters is adapted for 4L-2L grid-connected converters. To this end, since every sector comprises 4 tetrahedra (see Fig. 2.3), the first step is to determine the sector in which $\boldsymbol{u}_{\mathrm{uc}}(k)$ is projected on the $\alpha\beta$-plane (namely $\mathcal{S}_{\ell_{\mathrm{op}}}$) as:

$$\ell_{\mathrm{op}} = \text{ floor } \left\{ \frac{3}{\pi} \tan^{-1} \left(\frac{u_{\mathrm{uc}}^{\beta}}{u_{\mathrm{uc}}^{\alpha}} \right) \right\} + 1. \tag{3.20}$$

Then, the duty cycle vector $\boldsymbol{d}_j$ is computed only for the four tetrahedra within $\mathcal{S}_{\ell_{\mathrm{op}}}$, i.e., for $j = 4(\ell_{\mathrm{op}} - 1) + \kappa$, with $\kappa \in \{1, \ldots 4\}$. Consequently, using (3.17) and (3.20), the conventional enumeration algorithm for which the closed-form solution (obtained from (3.18) and (3.19)) is evaluated can be reduced from 24 to only 4, certainly reducing the computational overhead of the control algorithm.

3.1.5 Tuning of the controller

The design of the tuning matrix $\boldsymbol{\Lambda}_u$ is straightforward. As shown in (3.17), $\boldsymbol{u}_{\mathrm{uc}}(k)$ is the weighted sum between the deadbeat and the steady-state control inputs. It follows that by choosing $\boldsymbol{\Lambda}_u = \mathbf{B}$, the resulting control action will put the same priority to the grid current tracking error and control effort. Thus, using a large tuning matrix $\boldsymbol{\Lambda}_u$ compared with $\mathbf{B}$, the converter will apply an average switching vector close to $\boldsymbol{u}_{\mathrm{ss}}(k)$, which leads to open-loop operation. Conversely, if $\boldsymbol{\Lambda}_u \approx 0$, the first term in the cost function (3.9) becomes predominant and, hence, the converter tends to synthesize the deadbeat control action $\boldsymbol{u}_{\mathrm{db}}(k)$ in (3.10), which increases the controller bandwidth. Consequently, by starting from the initial setting point given by $\boldsymbol{\Lambda}_{u0} = \mathbf{B}$, i.e.,

$$\Lambda_{u0} = \mathrm{diag}\left(\lambda_{u0}^{\alpha}, \lambda_{u0}^{\beta}, \lambda_{u0}^{\gamma}\right) = V_{\mathrm{dc}} T_{\mathrm{p}}\, \mathrm{diag}\left(L_f^{-1}, L_f^{-1}, L_\gamma^{-1}\right) \tag{3.21}$$

the tuning parameters $\lambda_u^{\alpha\beta\gamma}$ can be manipulated in order to reduce ($\lambda_u^{\alpha\beta\gamma} > \lambda_{u0}^{\alpha\beta\gamma}$) or increase ($\lambda_u^{\alpha\beta\gamma} < \lambda_{u0}^{\alpha\beta\gamma}$) the closed-loop dynamic. Notice that this controller setting allows one to tune the dynamic behavior of the grid current's $\alpha\beta\gamma$ components in a decoupled manner. This implies that, for instance, the proposed controller can regulate the positive-, negative-, and zero-sequence components of the grid currents with different closed-loop dynamics.

3.1.6 OSS Implementation

Aiming to determine the modulating signals $\boldsymbol{D}_{\mathrm{abcn}}^{\star} = \left[D_{\mathrm{a}}^{\star}\, D_{\mathrm{b}}^{\star}\, D_{\mathrm{c}}^{\star}\, D_{\mathrm{n}}^{\star}\right]^{\intercal} \in [0,1]^4$ that allow the converter to synthesize the desired OSS, namely $\boldsymbol{S}_{\mathrm{op}}$, the method introduced in [40] is adopted in this work. Thus, the desired modulating signals are computed according to:

$$\boldsymbol{D}_{\mathrm{abcn}}^{\star} = d_x^{\star} \boldsymbol{u}_{\mathrm{abcn},x}^{\star} + d_y^{\star} \boldsymbol{u}_{\mathrm{abcn},y}^{\star} + d_z^{\star} \boldsymbol{u}_{\mathrm{abcn},z}^{\star} + \frac{1}{2} d_0^{\star} \tag{3.22}$$

where $\boldsymbol{u}_{\mathrm{abcn},\Upsilon}^{\star}$ are the 4-leg switching positions that produce the active switching vectors comprising the optimal tetrahedron j_{op}. Fig. 3.3 shows an illustrative example of this method when the optimal tetrahedron is $\mathcal{T}_{j_{\mathrm{op}}} = (8, 12, 13)$. Note that, using this simple OSS implementation, the carrier-signal frequency imposes the switching frequency of the converter's semiconductors.

3.1.7 Kalman filter

To improve the controller performance, the well-known Kalman filter [41] is implemented. The Kalman filter is in other words a closed loop observer. It can be used to estimate state variables, but in this case it is applied to filter the current signal $\boldsymbol{i}_g$ that are being measured. This kind of observer has a discrete-nature, thus, the discrete model of the system needs to be used (equation (3.7)). Kalman filter implementation consists in adding to the discrete model the product of the error of the state estimation $\boldsymbol{e}(k) = \boldsymbol{x}(k) - \hat{\boldsymbol{x}}(k)$ and a gain $\mathbf{K}$ (in this case $\boldsymbol{x}(k) = \boldsymbol{i}_g(k)$ and $\hat{\boldsymbol{x}}(k) = \hat{\boldsymbol{i}}_g(k)$), thus:

$$\hat{\boldsymbol{i}}_{\mathrm{g}}(k{+}1) = \mathbf{A}\hat{i}_{\mathrm{g}}(k) + \mathbf{P}\boldsymbol{v}_{\mathrm{g}}(k) + \mathbf{B}\,\boldsymbol{u}_s(k) + \mathbf{K}e(k) \tag{3.23}$$

where $\mathbf{K} > 0$ is the only restriction to assure the convergence of the estimated variables. The value of the gain $\mathbf{K}$ is obtained by solving the Riccati's equation [41]. The advantage of using this kind of observer is that the estimated states correspond to the predicted variables as can be seen in (3.23). Therefore, this observer is used instead of equation (3.7). To avoid using extra processing time, the gain $\mathbf{K}$ is computed offline using the solver *idare* of MATLAB.

3.1.8 Computation of future references and grid voltage

As a consequence of the discrete nature of digital platforms and predictive control schemes [42] it becomes necessary to predict future grid-voltage values for two main reasons. First, to make the right prediction of the future current and second to avoid the delay generation in current reference. To do this two methods are used:

3.1.8.1 Vector angle compensation

Using the vector representation of the variables of a three-phase system it becomes easy to estimate their future values. In steady state, it can be assumed that the vector rotates at a constant angular speed ω and that the magnitude remains constant. In this way, the future angle of the vector at instant $k + \Delta t$ could be estimated as $\theta(k + \Delta t) = \theta(k) + \omega\Delta t$. Hence, the grid voltage estimation can be computed as:

$$\boldsymbol{v}_g(k + \Delta t) = |\boldsymbol{v}_g|e^{j\theta(k+\Delta t)} = |\boldsymbol{v}_g|e^{j(\theta(k)+\omega\Delta t)} \tag{3.24}$$

3.1.8.2 Lagrange extrapolation

The vector angle compensation is easy to implement, but it has the limitation that it can only be applied in variables that can be represented as a rotating vector. In the case of zero-sequence variables this is not possible. Therefore, a posible solution is to calculate the one-step-ahead prediction using the nth-order formula of Lagrange extrapolation [43]:

$$\hat{\mathrm{x}}(k+1) = \sum_{l=0}^{n} (-1)^{n-l} \left[\begin{array}{c} n+1 \\ l \end{array} \right] \mathrm{x}(k+l-n) \tag{3.25}$$

where $\hat{x}$ could be the zero-sequence current reference $i_g^{\star\gamma}$ or grid-voltage v_g^{γ}. For sinusoidal variables the second order ($n = 2$) formula is sufficient for a good performance of the extrapolation (Eq. (3.26)). Despite of the aforementioned, the performance of this method decreases against step changes of the variables.

$$\hat{\mathbf{x}}(k+1) = 3\mathbf{x}(k) - 3\mathbf{x}(k-1) + \mathbf{x}(k-2) \tag{3.26}$$

Chapter 4

Simulation and Experimental results

4.1 Matlab simulations

Simulations of the 4L-2L converter connected to the grid through a RL-filter were carried out using the softwares MATLAB 2021b and PLECS Blockset 4.5.8. These simulations were performed in order to validate the experimental results shown in the following sections. Besides, comparisons with traditional PR controller are made to demonstrate the features of the controller proposed in this work. The system parameters are summarized in Table 4.1. For better visualization of the main variables, the grid variables were normalized with respect to their base quantities, i.e., $V_B = \sqrt{2/3}V_{\mathrm{R}}$, $I_B = \sqrt{2}I_{\mathrm{R}}$.

To demonstrate the performance of the proposed control scheme several simulations were implemented. In all of them, a switching frequency of 7.5 [kHz] and a pf $=$ 1 were utilized. In Fig. 4.1a the system response to a step-change in $\alpha\beta\gamma$ current references is shown. It can be seen that the response of the system is fast and with good reference tracking in all control variables. The same simulation is performed twice changing the zero-sequence current reference with a sinusoidal reference of 250 [Hz] and a triangular reference, in Fig. 4.1b and Fig. 4.1c respectively. In these two tests is probed again that the proposed controller has a fast transient response and good reference tracking, regardless of the waveform of the reference current. It is worthily to highlight that all these tests were computed without changing any parameter of

Table 4.1: Parameters of the Experimental Setup

Rated values		Param.	Value	Controller
I_{R}	$10/\sqrt{2}$ A	L_f	5.0 mH	$\lambda_{u0}^{\alpha} = \frac{V_{\mathrm{dc,R}}}{L_f}T_{\mathrm{p}}$
V_{R}	$110\sqrt{3}$ V	L_n	2.5 mH	$\lambda_{u0}^{\alpha} = \frac{V_{\mathrm{dc,R}}}{L_f}T_{\mathrm{p}}$
$V_{\mathrm{dc,R}}$	365 V	R_f	0.5 Ω	$\lambda_{u0}^{\gamma} = \frac{V_{\mathrm{dc,R}}}{L_\gamma}T_{\mathrm{p}}$

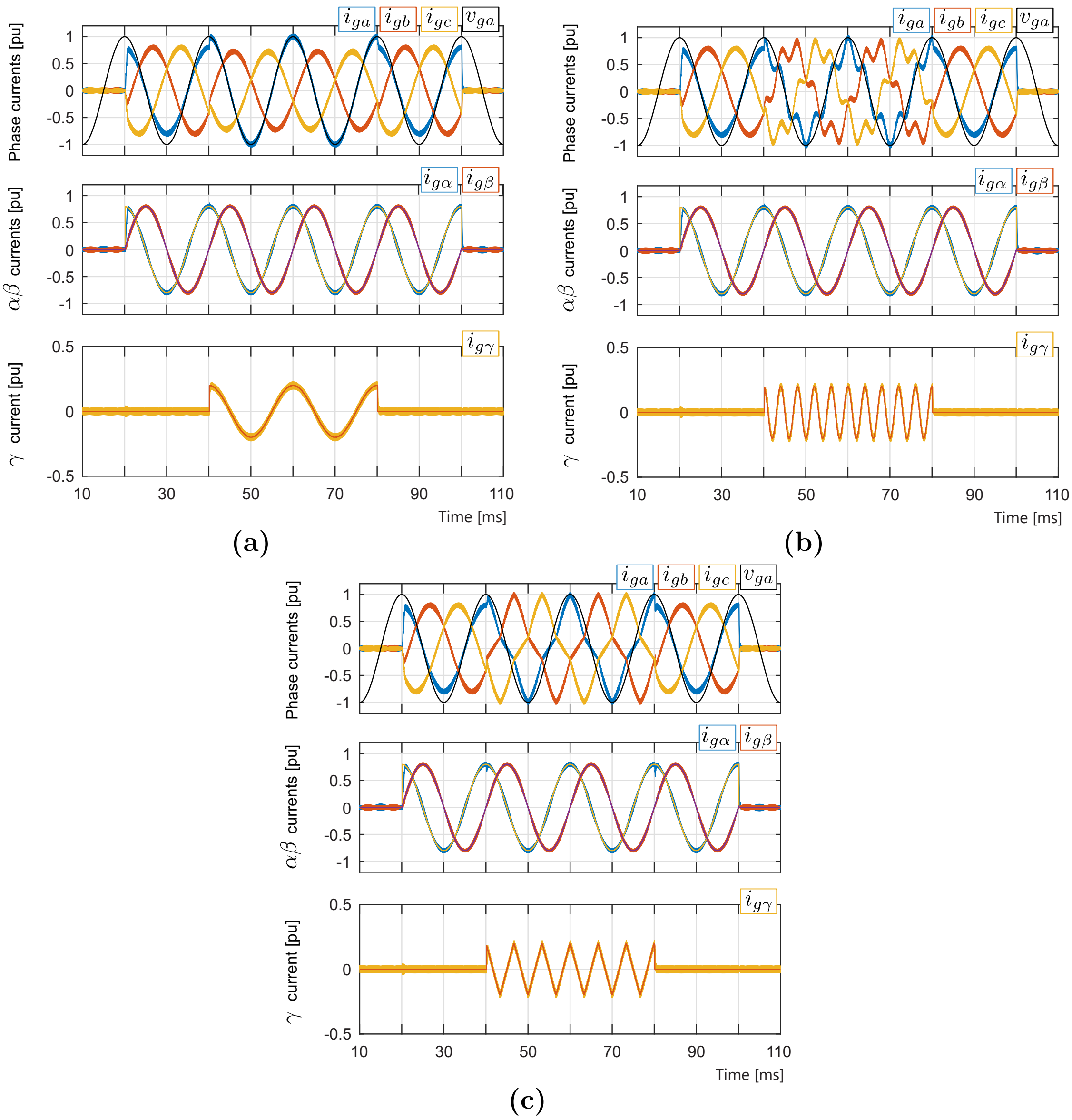

Figure 4.1: (a) Positive- and zero-sequence current step-changes, both at the fundamental frequency, (b) Zero-sequence current step-change of 250 Hz (c) sinusoidal and triangular references, respectively.

the controller, proving the versatility of the proposed MPC strategy.

The next simulations reveal the transient response of the proposed MPC scheme during a step change of the current reference. In Fig. 4.2a a whole fundamental cycle of the unconstrained voltage u_{uc} is displayed. Fig. 4.2b is a more detailed view of Fig. 4.2a. At an arbitrary instant of time the step response in current reference occurs producing that the controller actuation saturates. This simulation was carried out twice, first with the proposed saturation scheme determined in the previous chapter (equation (3.19)), next, the test was repeated using the Matlab solver **lsqlin** to compare if the results obtained with the proposed saturation scheme was optimal. The

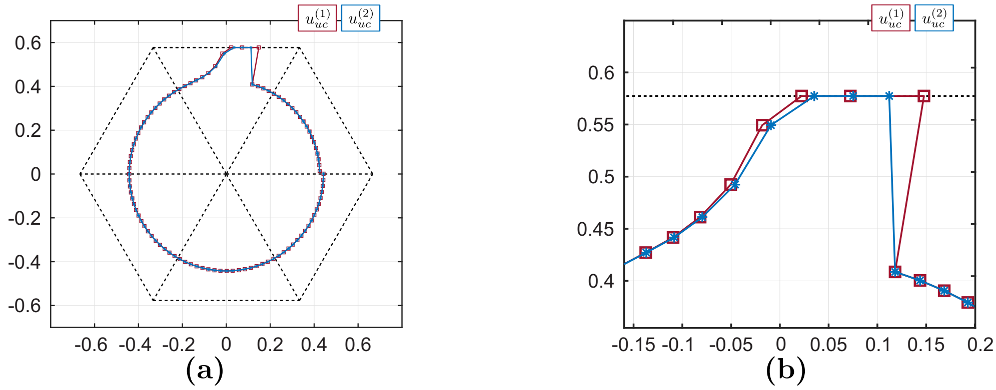

Figure 4.2: Transient response of the proposed MPC strategy. Superscripts (1) and (2) indicate that the stress unconstrained voltage u_{uc} was obtained with Matlab solver or with the the proposed strategy for saturated scenario (3.19), respectively. (a) u_{uc} response to step-change in $\alpha\beta$ current-references (b) Zoom of image in (a).

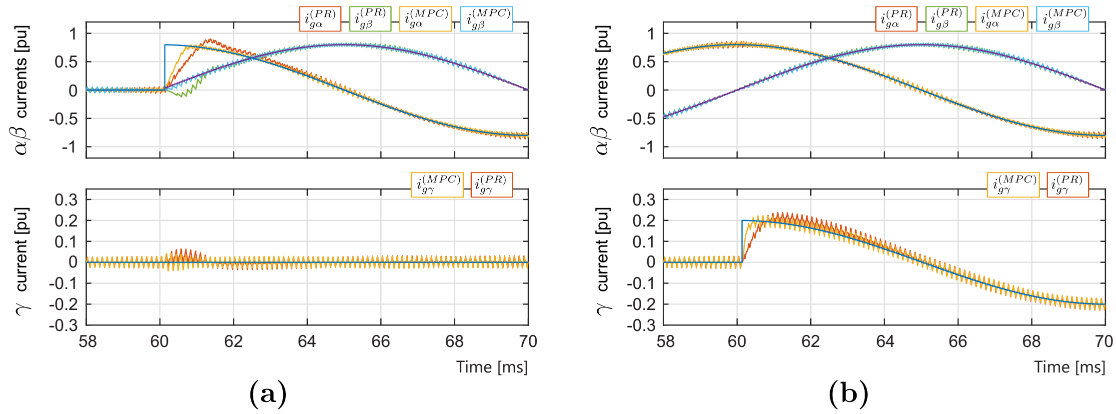

Figure 4.3: Comparison of the proposed MPC strategy and PR controller. (a) Step-change in $\alpha\beta$ currents and (b) Step-change in γ current.

results shown in Fig. 4.1a demonstrate that the method utilized is sub-optimal.

To conclude with the validation of the proposed method, a comparison is made with the traditional PR controller. In Fig. 4.3a and Fig. 4.3b, the response to step-change of current reference for both controllers is presented. It can be noticed that the the proposed MPC strategy has a faster dynamic response compared with traditional PR. This is due to the fact that the MPC strategy is able to take advantage of all the available actuation as it utilize the entire region of the hexagon generated by the states of the converter (Fig. 4.2a). In the 4L-2L converter the entire modulation region is the polyhedron shown in Fig. 2.3, the analysis is only made in $\alpha\beta$ plane to make the example easier, but the same idea can be extrapolated to the γ axis. In contrast with PR controller that it is only able to use the modulation region within the circumscribed circle in the hexagon.

Finally, to end this comparison, both controllers were tested against changes in

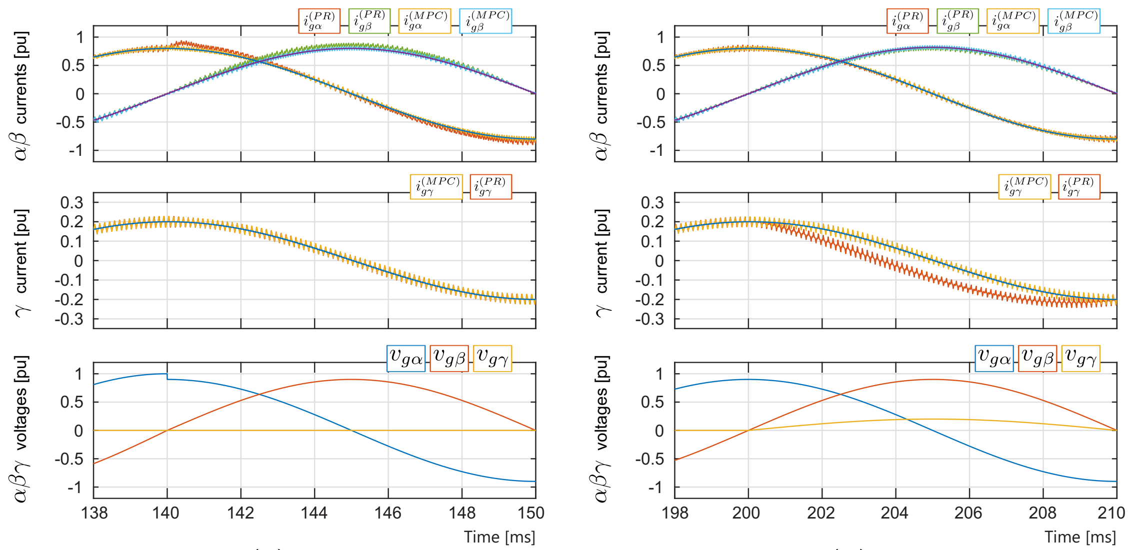

(a) **(b)**

Figure 4.4: Comparison of the proposed MPC strategy and PR controller. (a) Step-change in $\alpha\beta$ grid-voltages and (b) Step-change in γ grid-voltage.

the grid voltage. Fig. 4.4a presents the behaviour of the system under a step-change in $\alpha\beta$ voltage components of the grid. Again, the MPC strategy shows to be able to compensate this perturbation without even noticing an important change in the grid currents. Contrary to the PR controller, which shows a perturbation in the grid currents. This behavior is also visible in Fig. 4.4b where the system is tested under unbalanced grid voltages with the presence of zero-sequence voltage.

4.2 Experimental results

The performance of the proposed control strategy is evaluated in this section. To this end, the control algorithm was implemented in a DSP based on the DSK6713 platform augmented with a Xilinx FPGA Spartan 6-based board. The FPGA platform was programmed to handle the 12-bit analog-to-digital converters (ADC) and the carrier-based modulator to synthesize the desired OSS as explained in section 3.1.6. Experimental tests include steady-state and dynamic conditions for the grid-connected configuration. The system parameters are the same used in the simulations which were summarized in Table 4.1. Analogously to how it was done in the simulations section the grid variables were normalized with respect to their base quantities, i.e., V_B, I_B.

The laboratory setup used for the experimental results is the one shown in Fig. B.1 and Fig. B.2. A diagram of this setup is displayed in Fig. 4.5

4.2.1 Steady-State Performance

To evaluate the performance of the system, the TDD from equation (2.1) is utilized. The steady-state performance of the grid currents in the $\alpha\beta\gamma$ framework is shown in

Fig. 4.6. The switching frequency of the converter is set as $f_s = 5$ kHz. The amplitude references of the $\alpha\beta$ components are the rated current (namely, $I^{\alpha}_{g,\text{ref}} = I^{\beta}_{g,\text{ref}} = 10$ A), and the γ-component is $I^{\gamma}_{g,\text{ref}} = 5$ A. Fig. 4.6(a) shows the experimental waveforms operating with unity power factor (PF), meanwhile Fig. 4.6(b) is with PF $= 0$, injecting rated reactive power to the grid. For both cases, the injected current in the neutral is in phase to the neutral-to-line voltage v_{ga}. Besides, as observed in the second row of Fig. 4.6, the proposed MPC strategy imposes a shaped harmonic spectrum in which the amplitude of all harmonic components of the three-phase currents are below 3%, achieving, accordingly, a low TDD for both cases (on average 4.65% and 4.44%, respectively). Also, as depicted in these harmonic spectra, the high-frequency harmonic components are concentrated at 5 kHz, which corresponds to the carrier-signal frequency.

Fig. 4.7 shows the same steady-state performance validation as in Fig. 4.6, but using a higher switching frequency $f_s = 7.5$ kHz. As seen, the experimental results are similar since the amplitudes of the $\alpha\beta\gamma$-components are tracking the desired values. Still, the high-frequency harmonic components and the side-bands are centered at 7.5 kHz; meanwhile, the current TDD is reduced in the same proportion as the switching frequency increases (on average 3.19% and 3.06%, respectively). Additionally, Fig. 4.8 resumes the average value of the current TDD at rated current for different switching frequencies and power factors.

4.2.2 Effect of the Tuning Parameters.

In this section, four experiments were performed to demonstrate the effect of the tuning matrix $\mathbf{\Lambda}_u = \text{diag}(\lambda^{\alpha}_u, \lambda^{\beta}_u, \lambda^{\gamma}_u)$ on the dynamic performance of the controlled system. The switching frequency of the converter is set as 7.5 kHz. For all studied cases, sinusoidal references with rated amplitude are imposed for the $\alpha\beta$ components, i.e., $I^{\alpha\beta}_{g,\text{ref}} = 10$ A. In addition, the γ-component performance is evaluated under two signal references: a sinusoidal of fundamental frequency, and a triangular of 150 Hz with peak values of 5 A.

4.2.2.1 Tuning parameter $\lambda^{\alpha\beta}_u$

Fig. 4.9 and Fig. 4.10 compare the dynamic response of the grid currents for two different tuning parameters $\lambda^{\alpha\beta}_u$ when a step-change at instant $t = 0$ is applied. As

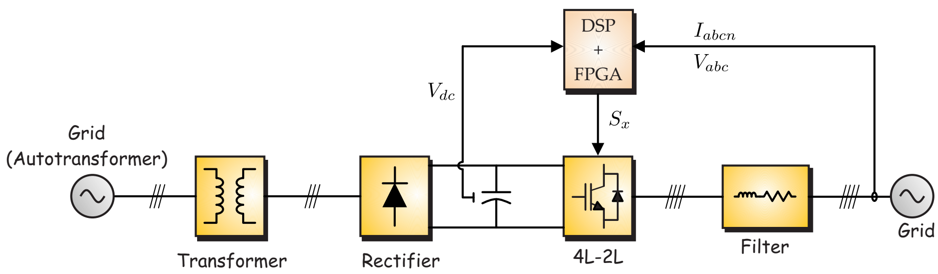

Figure 4.5: Laboratory setup diagram.

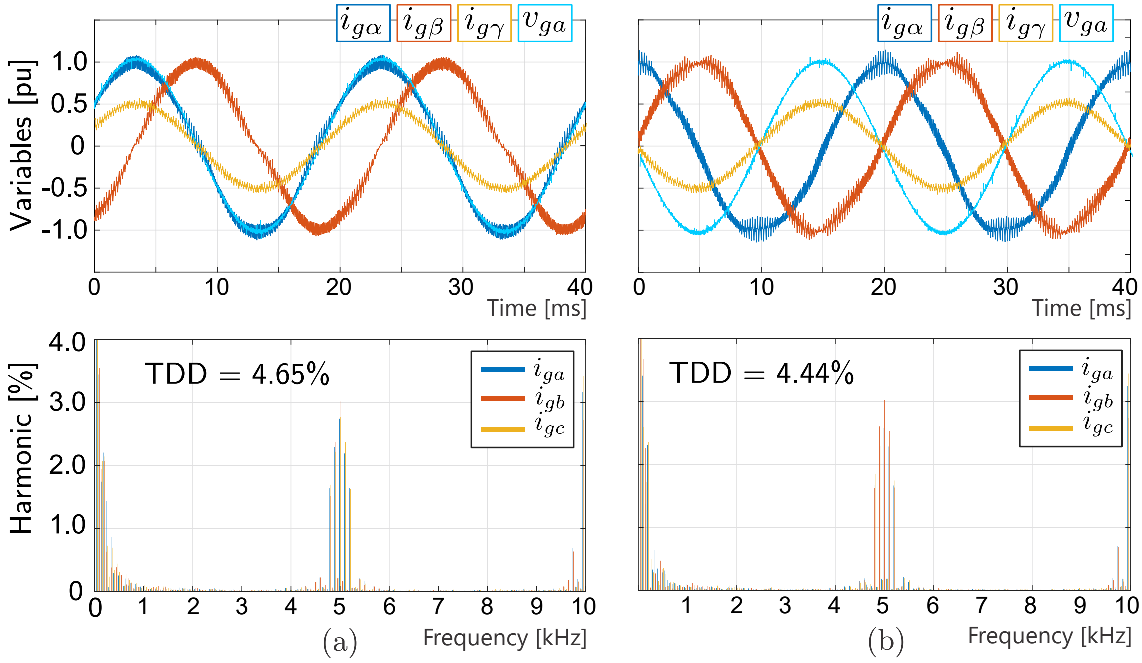

Figure 4.6: Steady-state performance at f_s=5 kHz: (a) PF=1; (b) PF = 0.

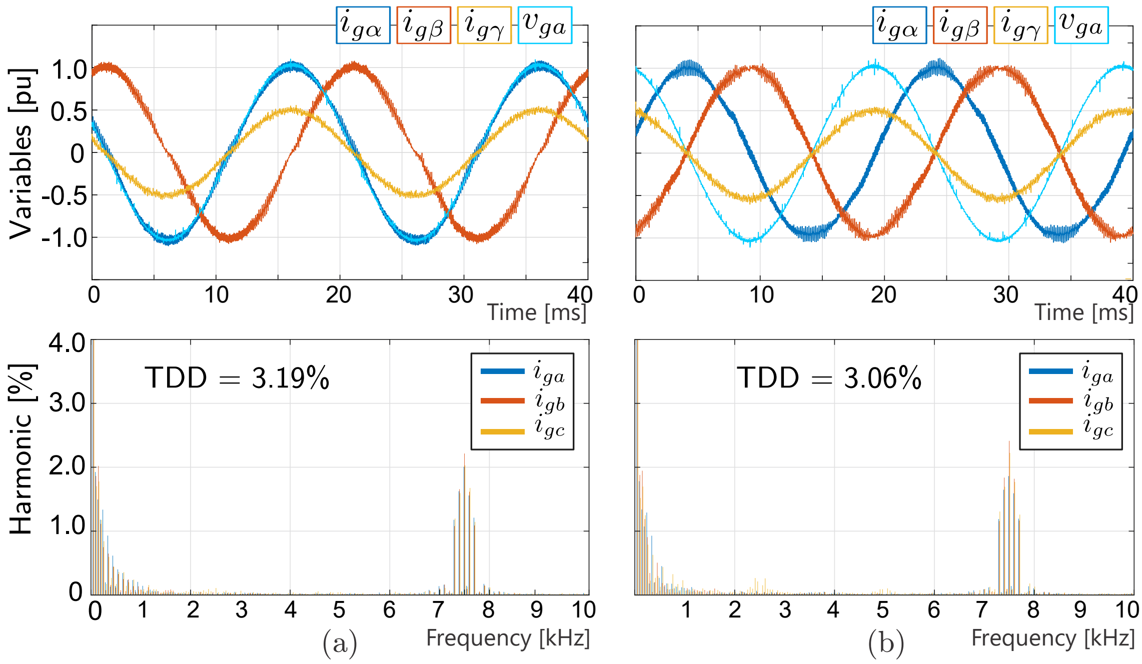

Figure 4.7: Steady-state performance at f_s=7.5 kHz: (a) PF =1; (b) PF = 0.

shown in these graphics, a lower value of $\lambda_u^{\alpha\beta}$ produces a more aggressive dynamic response with a slight overshoot during transients. Besides, the change of $\lambda_u^{\alpha\beta}$ does not impact on the transient response of current i_g^{γ}. This decoupled behavior is observed for the sinusoidal and triangular reference.

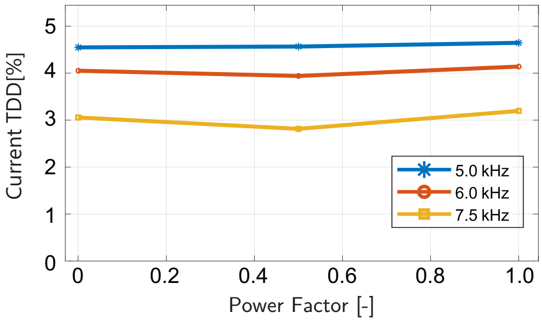

Figure 4.8: Experimental current TDD at rated power as function of the power factor for three switching frequencies.

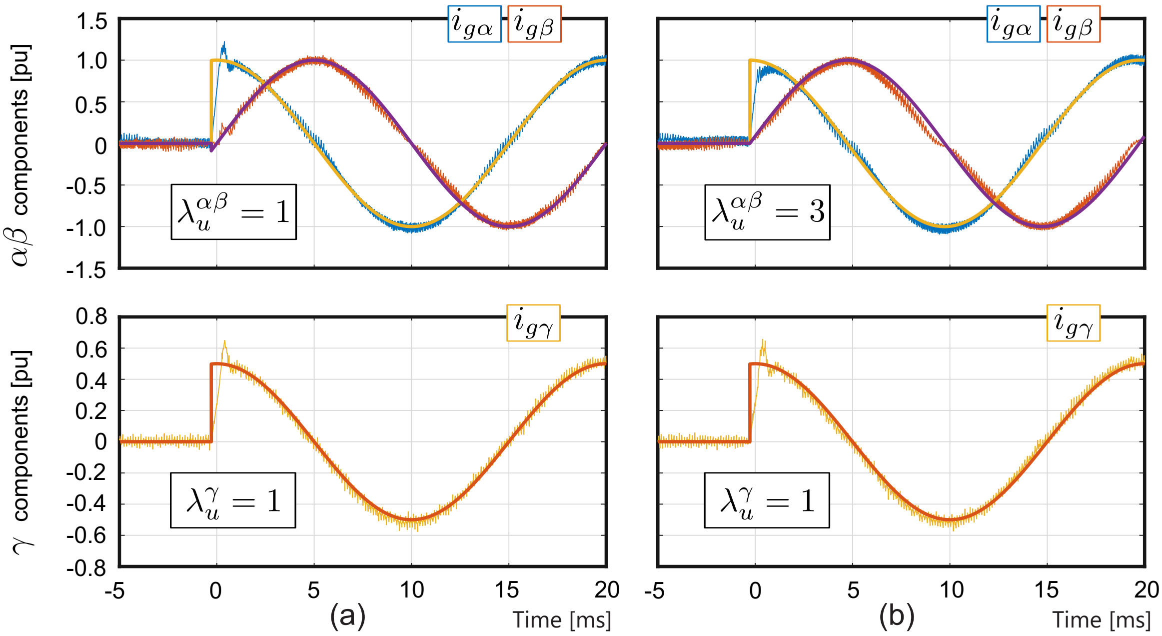

Figure 4.9: Effect of the tuning parameter $\lambda_u^{\alpha\beta}$ on the transient performance while keeping λ_u^{γ} constant: sinusoidal references.

4.2.2.2 Tuning parameter λ_u^{γ}

Analogously, Fig. 4.11 and Fig. 4.12 compare the dynamic response of the grid currents for two different tuning parameters λ_u^{γ}. As shown in these graphics, a lower value of λ_u^{γ} produces a more aggressive dynamic response but a better tracking of the triangular signal reference (see Fig. 4.12). Moreover, the experimental results depicted in these figures show exactly the same dynamic response for the $\alpha\beta$ components regardless of the value of λ_u^{γ} and the reference signal of current i_g^{γ}, demonstrating that the dynamic response of the $\alpha\beta$ components of the grid currents can be set in a decoupled manner of the γ component.

Notice the good tracking performance of the triangular waveform reference achieved in this subsection. These waveforms are not simple to track using conventional PI and PR controllers.

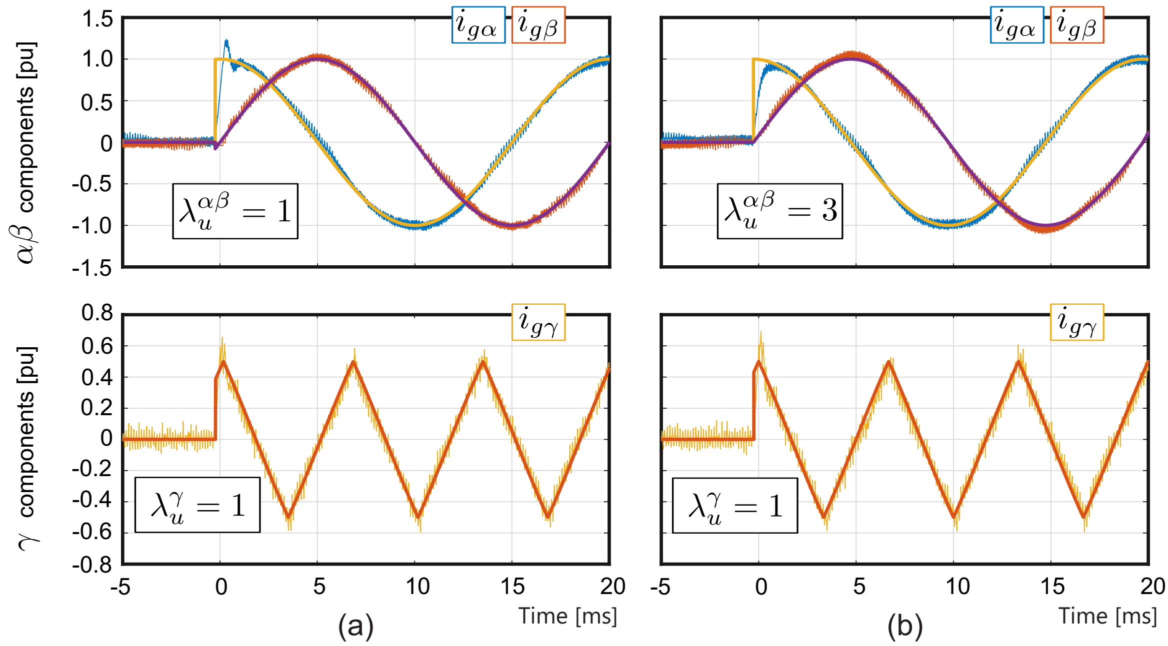

Figure 4.10: Effect of the tuning parameter $\lambda_u^{\alpha\beta}$ on the transient performance while keeping λ_u^{γ} constant: triangular reference for current i_g^{γ}.

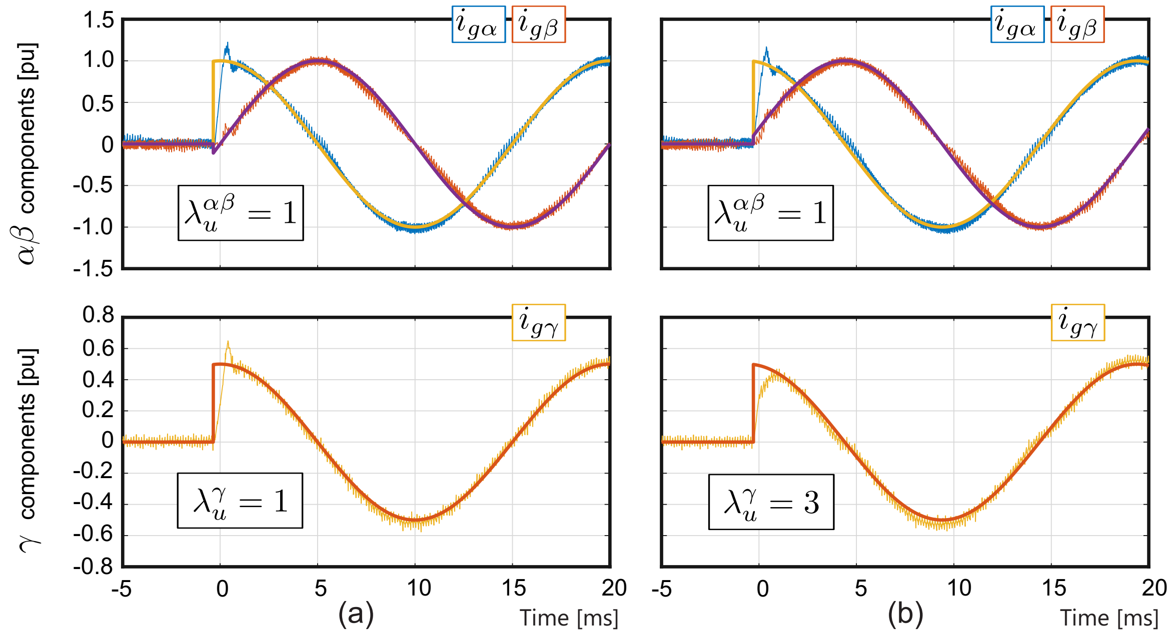

Figure 4.11: Effect of the tuning parameter λ_u^{γ} on the transient performance while keeping $\lambda_u^{\alpha\beta}$ constant: sinusoidal references.

4.2.3 Dynamic Performance.

Finally, two tests were performed to demonstrate adequate reference tracking in the presence of two different frequencies for the neutral current: 50 and 250 Hz. On the one hand, the behavior of the grid current is shown in Fig. 4.13a when reference step changes are imposed at different instants for the $\alpha\beta$ and γ components. Firstly,

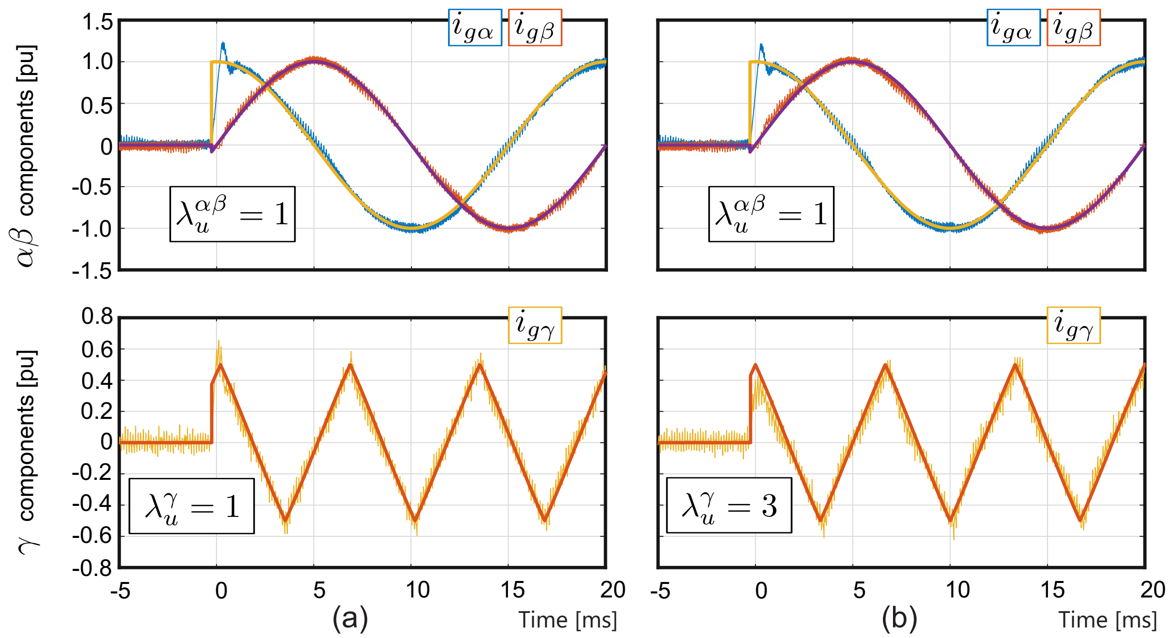

Figure 4.12: Effect of the tuning parameter λ_u^{γ} on the transient performance while keeping $\lambda_u^{\alpha\beta}$ constant: triangular reference for current i_g^{γ}.

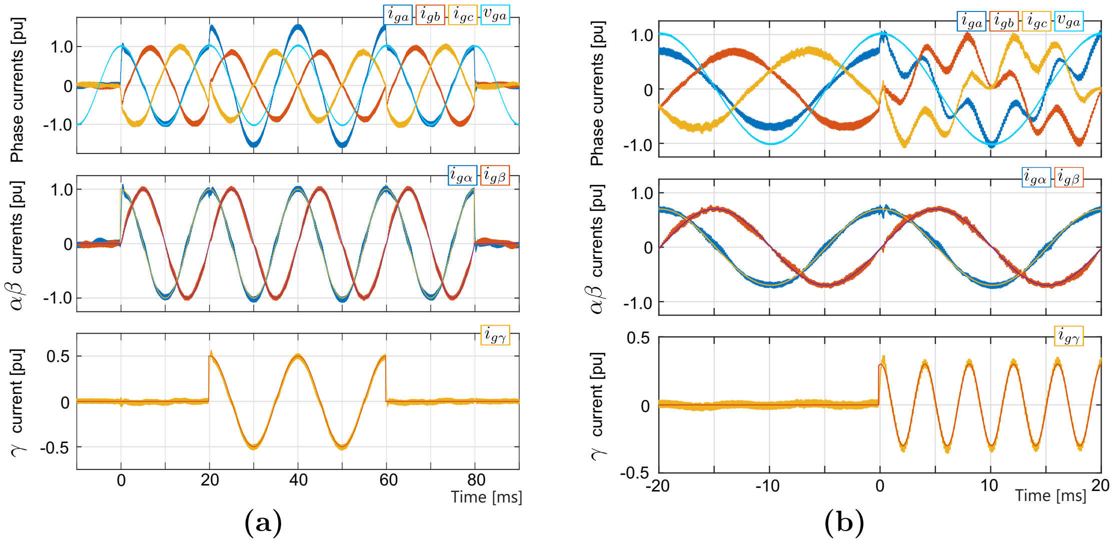

Figure 4.13: (a) Positive- and zero-sequence current step-changes, both at the fundamental frequency and (b) Zero-sequence current step-change of 250 Hz.

a rated positive-sequence current is injected at instant 0 seconds, and then, at instant 0.2 seconds, a zero-sequence current reference of amplitude 0.5 pu is included. On the other hand, the second test (Fig. 4.13b) demonstrates good tracking in the presence of a current in the neutral with a frequency equal to five times the fundamental. In both cases, a slight coupling between $\alpha\beta$ and γ current components arises when step-changes are applied in the command signals.

Chapter 5

Conclusions and future work

In this work, a MPC strategy based on optimal switching sequences is proposed for 4-leg grid-tied converters. Extensive experimental tests presented here have demonstrated that the proposed control method achieves a good performance in both steady-state and transient conditions, even for reference currents having high harmonic content.

The proposed OSS-MPC controller imposes the converter to operate with a fixed switching frequency and a predefined harmonic spectrum without compromising the inherent fast dynamic response of the predictive control strategies. In addition, users can tune the controller in a decoupled manner to establish different dynamic responses on the α, β, and γ components of the grid-currents. Therefore, the proposed controller is suitable for three-phase four-wire active-filter applications and distributed generation systems.

5.1 Future work

- Develop an alternative strategy for over-modulation stage based on the Active-Set method to achieve optimal results during this situations.
- Propose a method to minimize current ripple that works by changing the null-vectors application times (d_{0_P} and d_{0_N}), maintaining the restriction that $d_{0_P} + d_{0_N} = d_0$.
- Implement this strategy in a laboratory setup using a 4L-2L converter as an active filter to evaluate the performance of the proposed strategy in this situation.

Appendices

Chapter A

Table of tetrahedra and Switching Sequence's

Table A.1: Tretrahedrons gruped by sectors.

Sector	Tetrahedron	Active vectors	Switching Sequence $u_{s_{0N}}$	u_{s_x}	u_{s_y}	u_{s_z}	$u_{s_{0P}}$
S1	$\mathcal{R}_1$	u_1 u_9 u_{13}	0	0	1	1	1
			0	0	0	1	1
			0	0	0	0	1
			0	1	1	1	1
	$\mathcal{R}_2$	u_8 u_9 u_{13}	0	1	1	1	1
			0	0	0	1	1
			0	0	0	0	1
			0	0	1	1	1
	$\mathcal{R}_3$	u_8 u_{12} u_{13}	0	1	1	1	1
			0	0	1	1	1
			0	0	0	0	1
			0	0	0	1	1
	$\mathcal{R}_4$	u_8 u_{12} u_{14}	0	1	1	1	1
			0	0	1	1	1
			0	0	0	1	1
			0	0	0	0	1
S2	$\mathcal{R}_5$	u_1 u_5 u_{13}	0	0	0	1	1
			0	0	1	1	1
			0	0	0	0	1
			0	1	1	1	1
	$\mathcal{R}_6$	u_4 u_5 u_{13}	0	0	0	1	1
			0	1	1	1	1
			0	0	0	0	1
			0	0	1	1	1
	$\mathcal{R}_7$	u_4 u_{12} u_{13}	0	0	1	1	1
			0	1	1	1	1
			0	0	0	0	1
			0	0	0	1	1
	$\mathcal{R}_8$	u_4 u_{12} u_{14}	0	0	1	1	1
			0	1	1	1	1
			0	0	0	1	1
			0	0	0	0	1

Continuance of previous table

Sector	Tetrahedron	Active vectors	Switching Sequence				
			$u_{s_{0N}}$	u_{s_x}	u_{s_y}	u_{s_z}	$u_{s_{0P}}$
S3	$\mathcal{R}_9$	u_1 u_5 u_7	0	0	0	0	1
			0	0	1	1	1
			0	0	0	1	1
			0	1	1	1	1
	$\mathcal{R}_{10}$	u_4 u_5 u_7	0	0	0	0	1
			0	0	1	1	1
			0	1	0	1	1
			0	0	1	1	1
	$\mathcal{R}_{11}$	u_4 u_6 u_7	0	0	0	0	1
			0	1	1	1	1
			0	0	1	1	1
			0	0	0	1	1
	$\mathcal{R}_{12}$	u_4 u_6 u_{14}	0	0	0	1	1
			0	1	1	1	1
			0	0	1	1	1
			0	0	0	0	1
S4	$\mathcal{R}_{13}$	u_1 u_3 u_7	0	0	0	0	1
			0	0	0	1	1
			0	0	1	1	1
			0	1	1	1	1
	$\mathcal{R}_{14}$	u_2 u_3 u_7	0	0	0	0	1
			0	0	0	1	1
			0	1	1	1	1
			0	0	1	1	1
	$\mathcal{R}_{15}$	u_2 u_6 u_7	0	0	0	0	1
			0	0	1	1	1
			0	1	1	1	1
			0	0	0	1	1
	$\mathcal{R}_{16}$	u_2 u_6 u_{14}	0	0	0	1	1
			0	0	1	1	1
			0	1	1	1	1
			0	0	0	0	1

Continuance of previous table

Sector	Tetrahedron	Active vectors	Switching Sequence $u_{s_{0N}}$	u_{s_x}	u_{s_y}	u_{s_z}	$u_{s_{0P}}$
S5	$\mathcal{R}_{17}$	u_1 u_3 u_{11}	0	0	0	1	1
			0	0	0	0	1
			0	0	1	1	1
			0	1	1	1	1
	$\mathcal{R}_{18}$	u_2 u_3 u_{11}	0	0	0	1	1
			0	0	0	0	1
			0	1	1	1	1
			0	0	1	1	1
	$\mathcal{R}_{19}$	u_2 u_{10} u_{11}	0	0	1	1	1
			0	0	0	0	1
			0	1	1	1	1
			0	0	0	1	1
	$\mathcal{R}_{20}$	u_2 u_{10} u_{14}	0	0	1	1	1
			0	0	0	1	1
			0	1	1	1	1
			0	0	0	0	1
S6	$\mathcal{R}_{21}$	u_1 u_9 u_{11}	0	0	1	1	1
			0	0	0	0	1
			0	0	0	1	1
			0	1	1	1	1
	$\mathcal{R}_{22}$	u_8 u_9 u_{11}	0	1	1	1	1
			0	0	0	0	1
			0	0	0	1	1
			0	0	1	1	1
	$\mathcal{R}_{23}$	u_8 u_{10} u_{11}	0	1	1	1	1
			0	0	0	0	1
			0	0	1	1	1
			0	0	0	1	1
	$\mathcal{R}_{24}$	u_8 u_{10} u_{14}	0	1	1	1	1
			0	0	0	1	1
			0	0	1	1	1
			0	0	0	0	1

Chapter B

Images of Laboratory Setup

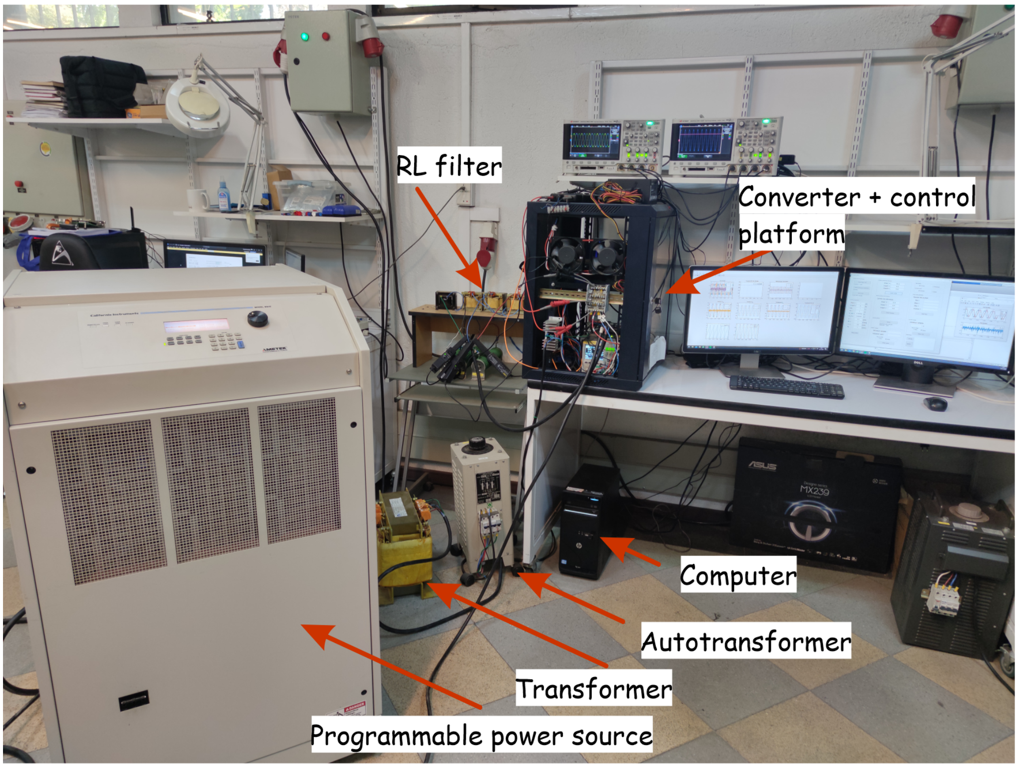

Figure B.1: Laboratory setup used for empirical results.

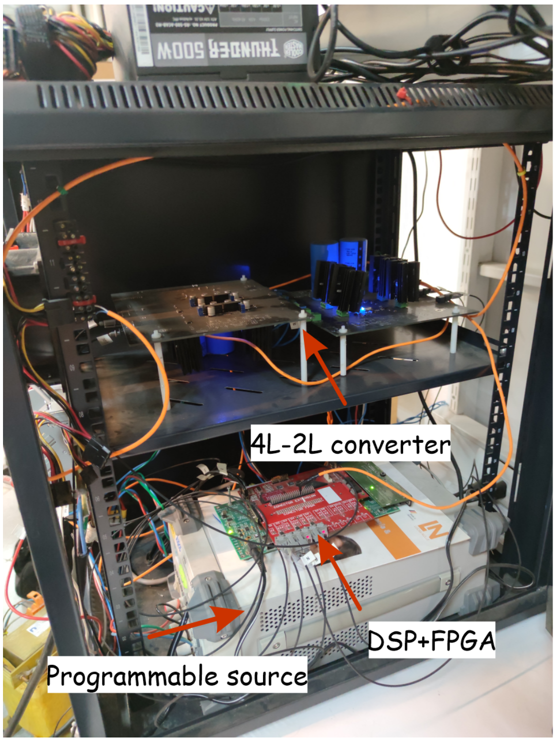

Figure B.2: Inside of the rack used to store the converter and control platform.

Bibliography

[1] S. Vazquez, J. Rodriguez, M. Rivera, L. G. Franquelo, and M. Norambuena, “Model Predictive Control for Power Converters and Drives: Advances and Trends,” *IEEE Transactions on Industrial Electronics*, vol. 64, no. 2, pp. 935–947, 2017.

[2] “IEEE Recommended Practice and Requirements for Harmonic Control in Electric Power Systems,” *IEEE Std 519-2014 (Revision of IEEE Std 519-1992)*, pp. 1–29, 2014.

[3] R. Wang, *Intelligent microgrid management and EV control under uncertainties in smart grid.* Springer, 2018.

[4] M. A. Hossain, H. R. Pota, M. J. Hossain, and F. Blaabjerg, “Evolution of microgrids with converter-interfaced generations: Challenges and opportunities,” *International Journal of Electrical Power & Energy Systems*, vol. 109, pp. 160–186, 2019.

[5] J. Fang, H. Li, Y. Tang, and F. Blaabjerg, “Distributed Power System Virtual Inertia Implemented by Grid-Connected Power Converters,” *IEEE Transactions on Power Electronics*, vol. 33, no. 10, pp. 8488–8499, 2018.

[6] E. Espina, J. Llanos, C. Burgos-Mellado, R. Cardenas-Dobson, M. Martinez-Gomez, and D. Saez, “Distributed Control Strategies for Microgrids: An Overview,” *IEEE Access*, vol. 8, pp. 193 412–193 448, 2020.

[7] T. Gönen, *Electric Power Distribution Engineering.* CRC Press, 2014.

[8] M. Z. Kamh and R. Iravani, “Unbalanced Model and Power-Flow Analysis of Microgrids and Active Distribution Systems,” *IEEE Trans. Power Del.*, vol. 25, no. 4, pp. 2851–2858, Oct 2010.

[9] V. Yaramasu, M. Rivera, B. Wu, and J. Rodriguez, “Model Predictive Current Control of Two-Level Four-Leg Inverters – Part I: Concept, Algorithm, and Simulation Analysis,” *IEEE Transactions on Power Electronics*, vol. 28, no. 7, pp. 3459–3468, July 2013.

[10] A. Mora, R. Cárdenas, M. Urrutia, M. Espinoza, and M. Díaz, "A Vector Control Strategy to Eliminate Active Power Oscillations in Four-Leg Grid-Connected Converters Under Unbalanced Voltages," *IEEE Journal of Emerging and Selected Topics in Power Electronics*, vol. 8, no. 2, pp. 1728–1738, 2020.

[11] P. Acuña, L. Morán, M. Rivera, J. Dixon, and J. Rodriguez, "Improved Active Power Filter Performance for Renewable Power Generation Systems," *IEEE Transactions on Power Electronics*, vol. 29, no. 2, pp. 687–694, Feb 2014.

[12] K. Antoniewicz, M. Jasinski, M. P. Kazmierkowski, and M. Malinowski, "Model Predictive Control for Three-Level Four-Leg Flying Capacitor Converter Operating as Shunt Active Power Filter," *IEEE Transactions on Industrial Electronics*, vol. 63, no. 8, pp. 5255–5262, 2016.

[13] S. Jiao, K. R. Ramachandran Potti, K. Rajashekara, and S. K. Pramanick, "A Novel DROGI-Based Detection Scheme for Power Quality Improvement Using Four-Leg Converter Under Unbalanced Loads," *IEEE Transactions on Industry Applications*, vol. 56, no. 1, pp. 815–825, 2020.

[14] A. S. Vijay, S. Doolla, and M. C. Chandorkar, "Unbalance mitigation strategies in microgrids," *IET Power Electronics*, vol. 13, no. 9, pp. 1687–1710, 2020.

[15] M. A. Hossain, H. R. Pota, W. Issa, and M. J. Hossain, "Overview of AC Microgrid Controls with Inverter-Interfaced Generations," *Energies*, vol. 10, no. 9, 2017.

[16] R. Teodorescu, F. Blaabjerg, M. Liserre, and P. C. Loh, "Proportional-resonant controllers and filters for grid-connected voltage-source converters," *IEE Proceedings - Electric Power Applications*, vol. 153, no. 5, pp. 750–762, 2006.

[17] F. Rojas, R. Cardenas, J. Clare, M. Diaz, J. Pereda, and R. Kennel, "A Design Methodology of Multiresonant Controllers for High Performance 400 Hz Ground Power Units," *IEEE Transactions on Industrial Electronics*, vol. 66, no. 8, pp. 6549–6559, 2019.

[18] D. E. Quevedo, R. P. Aguilera, and T. Geyer, *Predictive control in power electronics and drives: basic concepts, theory, and methods.* Springer, 2014.

[19] P. Karamanakos, E. Liegmann, T. Geyer, and R. Kennel, "Model Predictive Control of Power Electronic Systems: Methods, Results, and Challenges," *IEEE Open Journal of Industry Applications*, vol. 1, pp. 95–114, 2020.

[20] J. Rodriguez, M. P. Kazmierkowski, J. R. Espinoza, P. Zanchetta, H. Abu-Rub, H. A. Young, and C. A. Rojas, "State of the Art of Finite Control Set Model Predictive Control in Power Electronics," *IEEE Trans. Ind. Informat.*, vol. 9, no. 2, pp. 1003–1016, may 2013.

[21] M. Rivera, V. Yaramasu, J. Rodriguez, and B. Wu, "Model Predictive Current Control of Two-Level Four-Leg Inverters – Part II: Experimental Implementation

and Validation," *IEEE Transactions on Power Electronics*, vol. 28, no. 7, pp. 3469–3478, 2013.

[22] M. Rivera, V. Yaramasu, A. Llor, J. Rodriguez, B. Wu, and M. Fadel, "Digital Predictive Current Control of a Three-Phase Four-Leg Inverter," *IEEE Transactions on Industrial Electronics*, vol. 60, no. 11, pp. 4903–4912, Nov 2013.

[23] T. Geyer, "A Comparison of Control and Modulation Schemes for Medium-Voltage Drives: Emerging Predictive Control Concepts Versus PWM-Based Schemes," *IEEE Transactions on Industry Applications*, vol. 47, no. 3, pp. 1380–1389, 2011.

[24] J. Rodriguez, C. Garcia, A. Mora, S. A. Davari, J. Rodas, D. F. Valencia, M. Elmorshedy, F. Wang, K. Zuo, L. Tarisciotti, F. Flores-Bahamonde, W. Xu, Z. Zhang, Y. Zhang, M. Norambuena, A. Emadi, T. Geyer, R. Kennel, T. Dragicevic, D. A. Khaburi, Z. Zhang, M. Abdelrahem, and N. Mijatovic, "Latest Advances of Model Predictive Control in Electrical Drives – Part II: Applications and Benchmarking With Classical Control Methods," *IEEE Transactions on Power Electronics*, vol. 37, no. 5, pp. 5047–5061, 2022.

[25] P. Cortes, J. Rodriguez, C. Silva, and A. Flores, "Delay Compensation in Model Predictive Current Control of a Three-Phase Inverter," *IEEE Transactions on Industrial Electronics*, vol. 59, no. 2, pp. 1323–1325, 2012.

[26] F. Wang, L. He, and J. Rodriguez, "FPGA-Based Continuous Control Set Model Predictive Current Control for PMSM System Using Multistep Error Tracking Technique," *IEEE Transactions on Power Electronics*, vol. 35, no. 12, pp. 13 455–13 464, 2020.

[27] R. P. Aguilera, P. Lezana, and D. E. Quevedo, "Finite-Control-Set Model Predictive Control With Improved Steady-State Performance," *IEEE Transactions on Industrial Informatics*, vol. 9, no. 2, pp. 658–667, 2013.

[28] R. P. Aguilera and D. E. Quevedo, "Predictive Control of Power Converters: Designs With Guaranteed Performance," *IEEE Transactions on Industrial Informatics*, vol. 11, no. 1, pp. 53–63, feb 2015.

[29] J. M. Carrasco, L. G. Franquelo, J. T. Bialasiewicz, E. Galván, R. C. PortilloGuisado, M. M. Prats, J. I. León, and N. Moreno-Alfonso, "Power-electronic systems for the grid integration of renewable energy sources: A survey," *IEEE Transactions on industrial electronics*, vol. 53, no. 4, pp. 1002–1016, 2006.

[30] H. Akagi, E. H. Watanabe, and M. Aredes, *Instantaneous Power Theory and Applications to Power Conditioning.* Wiley-IEEE Press, 2017.

[31] H. Akagi, "Trends in active power line conditioners," *IEEE transactions on power electronics*, vol. 9, no. 3, pp. 263–268, 1994.

[32] F. Rojas, R. Cárdenas, R. Kennel, J. C. Clare, and M. Díaz, “A Simplified Space-Vector Modulation Algorithm for Four-Leg NPC Converters,” *IEEE Transactions on Power Electronics*, vol. 32, no. 11, pp. 8371–8380, 2017.

[33] P. Karamanakos and T. Geyer, “Guidelines for the Design of Finite Control Set Model Predictive Controllers,” *IEEE Transactions on Power Electronics*, vol. 35, no. 7, pp. 7434–7450, 2020.

[34] L. M. A. Caseiro, A. M. S. Mendes, and S. M. A. Cruz, “Dynamically Weighted Optimal Switching Vector Model Predictive Control of Power Converters,” *IEEE Transactions on Industrial Electronics*, vol. 66, no. 2, pp. 1235–1245, 2019.

[35] A. Mora, R. Cardenas-Dobson, R. P. Aguilera, A. Angulo, F. Donoso, and J. Rodriguez, “Computationally Efficient Cascaded Optimal Switching Sequence MPC for Grid-Connected Three-Level NPC Converters,” *IEEE Transactions on Power Electronics*, vol. 34, no. 12, pp. 12 464–12 475, Dec 2019.

[36] S. Vazquez, A. Marquez, R. Aguilera, D. Quevedo, J. I. Leon, and L. G. Franquelo, “Predictive Optimal Switching Sequence Direct Power Control for Grid-Connected Power Converters,” *IEEE Transactions on Industrial Electronics*, vol. 62, no. 4, pp. 2010–2020, April 2015.

[37] S. A. Larrinaga, M. A. R. Vidal, E. Oyarbide, and J. R. T. Apraiz, “Predictive Control Strategy for DC/AC Converters Based on Direct Power Control,” *IEEE Transactions on Industrial Electronics*, vol. 54, no. 3, pp. 1261–1271, June 2007.

[38] S. Vazquez, P. Acuna, R. P. Aguilera, J. Pou, J. I. Leon, and L. G. Franquelo, “DC-Link Voltage Balancing Strategy Based on Optimal Switching Sequences Model Predictive Control for Single-Phase H-NPC Converters,” *IEEE Transactions on Industrial Electronics*, pp. 1–1, 2019.

[39] F. Donoso, A. Mora, R. Cardenas, A. Angulo, D. Saez, and M. Rivera, “Finite-Set Model-Predictive Control Strategies for a 3L-NPC Inverter Operating With Fixed Switching Frequency,” *IEEE Transactions on Industrial Electronics*, vol. 65, no. 5, pp. 3954–3965, May 2018.

[40] X. Li, Z. Deng, Z. Chen, and Q. Fei, “Analysis and Simplification of Three-Dimensional Space Vector PWM for Three-Phase Four-Leg Inverters,” *IEEE Transactions on Industrial Electronics*, vol. 58, no. 2, pp. 450–464, 2011.

[41] D. Simon, *Optimal State Estimation: Kalman, H Infinity, and Nonlinear Approaches.* Wiley, 2006. [Online]. Available: https://books.google.cl/books?id=UiMVoP_7TZkC

[42] J. Rodriguez and P. Cortes, *Predictive Control of Power Converters and Electrical Drives.* Wiley-IEEE Press, 2012.

[43] O. Kukrer, “Discrete-time current control of voltage-fed three-phase pwm inverters,” *IEEE Transactions on Power Electronics*, vol. 11, no. 2, pp. 260–269, 1996.